Part I

Morphology and dynamics of the large-scale structure

Chapter 1

Cosmological perturbations and structure formation

Contents

1.1 The homogeneous Universe **8**
1.2 Statistical description of cosmological fields **9**
1.2.1 Average and ergodicity 9
1.2.2 Statistical homogeneity and isotropy 9
1.2.3 Gaussian and log-normal random fields in cosmostatistics 10
1.2.4 Correlation functions and power spectra 12
1.3 Dynamics of gravitational instability **15**
1.3.1 The Vlasov-Poisson system 16
1.3.2 Fluid dynamics approach, evolution equations in phase space 17
1.3.3 The single-stream approximation 18
1.4 Eulerian perturbation theory **18**
1.4.1 Eulerian linear perturbation theory 18
1.4.2 The growth of fluctuations in linear theory 19
1.4.3 Eulerian perturbation theory at higher order 21
1.5 Lagrangian perturbation theory **22**
1.5.1 Lagrangian fluid approach for cold dark matter 22
1.5.2 The Zel'dovich approximation 23
1.5.3 Second-order Lagrangian perturbation theory 24
1.6 Non-linear approximations to gravitational instability **25**
1.6.1 The Zel'dovich approximation as a non-linear approximation 25
1.6.2 Other velocity potential approximations 26
1.6.3 The adhesion approximation 26

> "For the mind wants to discover by reasoning what exists in the infinity of space that lies out there, beyond the ramparts of this world – that region into which the intellect longs to peer and into which the free projection of the mind does actually extend its flight."
> — Lucretius, *De Rerum Natura*

Abstract

This chapter provides an overview of the current paradigm of cosmic structure formation, as relevant for this thesis. It also reviews standard tools for large-scale structure analysis.

This chapter is organized as follows. In section 1.1, key equations of general relativistic Friedmann-Lemaître cosmological models are briefly reviewed, followed by a discussion of the statistical description of cosmological fields in section 1.2 and of the dynamics of gravitational instability in section 1.3. In section 1.4 and 1.5 we describe cosmological perturbation theory in Eulerian and Lagrangian descriptions. Finally, section 1.6 deals with various non-linear approximations to gravitational instability.

1.1 The homogeneous Universe

This section provides an overview of the standard picture of cosmology, describing the homogeneous evolution of the Universe. In particular, we reproduce some very standard equations around which perturbation theory will be implemented in the following. A demonstration can be found in any introduction to cosmology, see for example Peebles (1980); Kolb & Turner (1990); Liddle & Lyth (2000); Bernardeau *et al.* (2002); Lesgourgues (2004); Trodden & Carroll (2004); Langlois (2005, 2010).

Let a be the cosmic scale factor, normalized to unity at the present time: $a_0 = 1$. We denote by t the cosmic time, by τ the conformal time, defined by $\mathrm{d}t = a(\tau)\,\mathrm{d}\tau$, and by z the redshift, defined by $a = 1/(1+z)$. In the following, a dot denotes a differentiation with respect to t and a prime a differentiation with respect to τ. Friedmann's equations, describing the dynamics of the Universe, are derived from Einstein's equations of general relativity. In conformal time, they read:

$$\mathcal{H}^2 = \frac{8\pi \mathrm{G}}{3} a^2 \rho - k, \tag{1.1}$$

$$\text{and} \quad \mathcal{H}' = -\frac{4\pi \mathrm{G}}{3} a^2 (\rho + 3P), \tag{1.2}$$

where $\mathcal{H} \equiv a'/a = aH$ is the conformal expansion rate, $H \equiv \dot{a}/a$ is the Hubble parameter, ρ the total energy density and P the pressure. k is the reduced curvature parameter, taking one of the following values: -1 for an open universe, 0 for a flat universe, 1 for a closed universe. G denotes the gravitational constant, and we adopt units such that $\mathrm{c} = 1$.

As a direct consequence, Friedmann's equations immediately determine the evolution of the energy density, described as:

$$\rho' = -3\mathcal{H}(\rho + P). \tag{1.3}$$

Throughout this thesis, we will particularly focus on the eras of matter domination and dark-energy domination within the standard ΛCDM paradigm. Hence, we will consider that the content of the Universe is limited to two components: matter (mostly cold dark matter) and dark energy in the form of a cosmological constant Λ. We denote by ρ_m and $\rho_\Lambda \equiv \Lambda/8\pi\mathrm{G}$ their respective energy densities. Introducing their respective equations of state, $w_i \equiv P_i/\rho_i$, we have $w \approx 0$ for cold dark matter and $w = -1$ for the cosmological constant. For this cosmology, equation (1.2) reads

$$\mathcal{H}' = -\frac{4\pi \mathrm{G}}{3} a^2 \rho_\mathrm{m} + \frac{8\pi \mathrm{G}}{3} a^2 \rho_\Lambda. \tag{1.4}$$

It is convenient to introduce the dimensionless cosmological parameters as the ratio of density to critical density, $\rho_\mathrm{crit}(t) \equiv 3H^2(t)/8\pi\mathrm{G}$, which corresponds to the total energy density in a flat universe: $\Omega_\mathrm{m}(t) \equiv 8\pi\mathrm{G}\rho_\mathrm{m}(t)/3H^2(t)$ and $\Omega_\Lambda(t) \equiv 8\pi\mathrm{G}\rho_\Lambda/3H^2(t) = \Lambda/3H^2(t)$. Their expression in terms of conformal time is given by

$$\Omega_\mathrm{m}(\tau)\mathcal{H}^2(\tau) = \frac{8\pi \mathrm{G}}{3} \rho_\mathrm{m}(\tau) a^2(\tau), \tag{1.5}$$

$$\Omega_\Lambda(\tau)\mathcal{H}^2(\tau) = \frac{8\pi \mathrm{G}}{3} \rho_\Lambda a^2(\tau) \equiv \frac{\Lambda}{3} a^2(\tau). \tag{1.6}$$

Note that $\Omega_\mathrm{m}(\tau)$ and $\Omega_\Lambda(\tau)$ are time-dependent. Inserting these two expressions in equation (1.4) yields the following form of the second Friedmann equation,

$$\mathcal{H}'(\tau) = \left(-\frac{\Omega_\mathrm{m}(\tau)}{2} + \Omega_\Lambda(\tau) \right) \mathcal{H}^2(\tau), \tag{1.7}$$

and the first one reads

$$\mathcal{H}^2 = \frac{8\pi \mathrm{G}}{3} a^2 \rho_\mathrm{m} + \frac{8\pi \mathrm{G}}{3} a^2 \rho_\Lambda - k = \Omega_\mathrm{m}\mathcal{H}^2 + \Omega_\Lambda \mathcal{H}^2 - k, \tag{1.8}$$

which yields

$$k = (\Omega_\mathrm{tot}(\tau) - 1)\mathcal{H}^2(\tau), \tag{1.9}$$

where $\Omega_\mathrm{tot}(\tau) \equiv \Omega_\mathrm{m}(\tau) + \Omega_\Lambda(\tau)$. In the following, we will note $\Omega_\mathrm{m}^{(0)} = \Omega_\mathrm{m}(a=1)$ and $\Omega_\Lambda^{(0)} = \Omega_\Lambda(a=1)$.

1.2 Statistical description of cosmological fields

In this section, we consider some cosmic scalar field $\lambda(\mathbf{x})$ whose statistical properties are to be described. It denotes either the cosmological density contrast, $\delta(\mathbf{x})$, the gravitational potential, $\Phi(\mathbf{x})$ (see section 1.3), or any other field of interest derived from vectorial fields (e.g. the velocity divergence field), polarization fields, etc.

As discussed in the introduction, values of $\lambda(\mathbf{x})$ have to be treated as stochastic variables. For an arbitrary number n of spatial positions $\mathbf{x}_i$, one can define the *joint multivariate probability distribution function* to have $\lambda(\mathbf{x}_1)$ between λ_1 and $\lambda_1 + \mathrm{d}\lambda_1$, $\lambda(\mathbf{x}_2)$ between λ_2 and $\lambda_2 + \mathrm{d}\lambda_2$, etc. This pdf is written

$$\mathcal{P}(\lambda_1, \lambda_2, ..., \lambda_n)\,\mathrm{d}\lambda_1 \mathrm{d}\lambda_2 \dots \mathrm{d}\lambda_n. \tag{1.10}$$

1.2.1 Average and ergodicity

Average. The word "average" (and in the following, the corresponding $\langle\rangle$ symbols) may have two different meanings. First, one can average by taking many realizations drawn from the distribution, all of them produced in the same way (e.g. by N-body simulations). This is the *ensemble average*, defined to be for any quantity $X(\lambda_1, \lambda_2, ..., \lambda_n)$:

$$\langle X \rangle \equiv \int X(\lambda_1, \lambda_2, ..., \lambda_n)\mathcal{P}(\lambda_1, \lambda_2, ..., \lambda_n)\,\mathrm{d}\lambda_1 \mathrm{d}\lambda_2 \dots \mathrm{d}\lambda_n, \tag{1.11}$$

where $\mathcal{P}(\lambda_1, \lambda_2, ..., \lambda_n)$ is the joint multivariate pdf.

One can also average by considering the quantity of interest at different locations within the same realization of the distribution. This is the *sample average*. For some volume V in the Universe, the sample average over V of a quantity X is defined to be:

$$\bar{X} \equiv \frac{1}{V} \int_V X(\mathbf{x})\,\mathrm{d}^3\mathbf{x}. \tag{1.12}$$

Ergodicity. If the ensemble average of any quantity coincides with the sample average of the same quantity, the system is said to be *ergodic*. In cosmology, the hypothesis of ergodicity is often adopted, at least if the considered catalogue is large enough. For instance, if ergodicity holds, the mean density of the Universe is given by

$$\langle \rho(\mathbf{x}) \rangle = \bar{\rho} \equiv \frac{1}{V} \int_V \rho(\mathbf{x})\,\mathrm{d}^3\mathbf{x}, \tag{1.13}$$

in the limit where $V \to \infty$. The term of ergodicity historically refers to time processes, not to spatial ones. If the above property is fulfilled in cosmology, one says that the system is a *fair sample* of the Universe.[1]

1.2.2 Statistical homogeneity and isotropy

A random field is said to be *statistically homogeneous* if all joint multivariate pdfs $\mathcal{P}(\lambda(\mathbf{x}_1), \lambda(\mathbf{x}_2), ..., \lambda(\mathbf{x}_n))$ are invariant under translations of the coordinates $\mathbf{x}_1$, $\mathbf{x}_2$, ..., $\mathbf{x}_n$ in space. Thus probabilities depend only on relative positions, but not on locations. Note that statistical homogeneity is a weaker assumption than homogeneity, which would mean that $\lambda(\mathbf{x})$ takes the same value everywhere in space.

Similarly, a random field is said to be *statistically isotropic* if all $\mathcal{P}(\lambda(\mathbf{x}_1), \lambda(\mathbf{x}_2), ..., \lambda(\mathbf{x}_n))$ are invariant under spatial rotations.

From now on, cosmic fields will be considered statistically homogeneous and isotropic, as a consequence of the cosmological principle that underlies most inflationary calculations (see Guth, 1981; Linde, 1982; Albrecht & Steinhardt, 1982; Linde, 1995), and of standard gravitational evolution (e.g. Peebles, 1980). Of course, the validity of this assumption has to be checked against observational data. It is also important to note that a lot of the information from galaxy surveys comes from effects that distort the observed signal away from this ideal. In particular, observational effects such as the Alcock-Paczynski effect (Alcock & Paczynski, 1979) and redshift-space distortions (Kaiser, 1987) in galaxy surveys introduce significant deviations from statistical homogeneity and isotropy.

[1] In the case of the LSS, care should be taken with deep surveys. Indeed, as data lie on the surface of the relativistic lightcone, we cannot have access to a fair sample of the Universe at the present time. Rigorously, ergodicity is not verified.

1.2.3 Gaussian and log-normal random fields in cosmostatistics

This section draws from subsection 2.2 of Leclercq, Pisani & Wandelt (2014).

Gaussian random fields are ubiquitous in cosmostatistics (see Lahav & Suto, 2004; Wandelt, 2013; Leclercq, Pisani & Wandelt, 2014, for reviews). Indeed, as mentioned in the introduction, inflationary models predict the initial density perturbations to arise from a large number of independent quantum fluctuations, and therefore to be very nearly Gaussian-distributed. Even in models which are said to produce "large" non-Gaussianities, deviations from Gaussianity are strongly constrained by observational tests (see Planck Collaboration, 2014b, 2015, for the latest results). Grfs are essential for the analysis of the cosmic microwave background, but the large scale distribution of galaxies can also be approximately modeled as a grf, at least on very large scales, where gravitational evolution is still well-described by linear perturbation theory (see sections 1.4 and 1.5). The log-normal distribution is convenient for modeling the statistical behavior of evolved density fields, partially accounting for non-linear gravitational effects at the level of the one-point distribution.

In the following, we summarize some results about finite-dimensional Gaussian and log-normal random fields. Without loss of generality, infinite-dimensional fields can be discretized. If the field is sufficiently regular and the discretization scale is small enough, no information will be lost. In practice, throughout this thesis, any field that we want to describe is already discretized on a grid of particles or voxels. Let us denote the values of the considered cosmic scalar field $\lambda(\mathbf{x})$ at comoving positions $\mathbf{x}_i$ as $\lambda_i \equiv \lambda(\mathbf{x}_i)$ for i from 1 to any arbitrary integer n.

1.2.3.1 Gaussian random fields

The n-dimensional vector $\lambda = (\lambda_i)_{1\leq i\leq n}$ is a Gaussian random field (we will often say "is Gaussian" in the following) with mean $\mu \equiv (\mu_i)_{1\leq i\leq n}$ and covariance matrix $C \equiv (C_{ij})_{1\leq i\leq n, 1\leq j\leq n}$ if its joint multivariate pdf is a multivariate Gaussian:[2]

$$\mathcal{P}(\lambda|\mu, C) = \frac{1}{\sqrt{|2\pi C|}} \exp\left(-\frac{1}{2}(\lambda-\mu)^* C^{-1}(\lambda-\mu)\right) = \frac{1}{\sqrt{|2\pi C|}} \exp\left(-\frac{1}{2}\sum_{i=1}^{n}\sum_{j=1}^{n}(\lambda_i-\mu_i)C^{-1}_{ij}(\lambda_j-\mu_j)\right). \tag{1.14}$$

where z^* denotes the conjugate transpose of z, vertical bars indicate the determinant of the surrounded matrix and C is assumed to be a positive-definite Hermitian matrix (and therefore invertible). In practical cases, μ is often taken to be zero. As can be seen from this definition, a grf is completely specified by its mean μ and its covariance matrix C.

It is interesting to note that for the density contrast $\delta(\mathbf{x})$, the Gaussian assumption has to break down at later epochs of structure formation since it predicts density amplitudes to be symmetrically distributed among positive and negative values, but weak and strong energy conditions require $\delta(\mathbf{x}) \geq -1$. Even in the initial conditions, Gaussianity can not be exact due to the existence of this lower bound. The Gaussian assumption is therefore strictly speaking only valid in the limit of infinitesimally small density fluctuations, $|\delta(\mathbf{x})| \ll 1$.

1.2.3.2 Moments of Gaussian random fields, Wick's theorem

From equation (1.14) it is easy to check that the mean $\langle\lambda\rangle$ is really μ and the covariance matrix is really $\langle(\lambda-\mu)^*(\lambda-\mu)\rangle = C$, just by evaluating the Gaussian integrals:

$$\langle\lambda_i\rangle = \int \lambda_i\, \mathcal{P}(\lambda|\mu, C)\, \mathrm{d}\lambda_i = \mu_i, \tag{1.15}$$

$$\langle(\lambda_i-\mu_i)^*(\lambda_j-\mu_j)\rangle = \int (\lambda_i-\mu_i)^*(\lambda_j-\mu_j)\, \mathcal{P}(\lambda|\mu, C)\, \mathrm{d}\lambda_i \mathrm{d}\lambda_j = C_{ij}. \tag{1.16}$$

We now want to compute higher-order moments of a grf. Let us focus on central moments, or equivalently, let us assume in the following that the mean is $\mu = 0$. Here we omit the star denoting conjugate transpose for simplicity. Any odd moments, e.g. the third $\langle\lambda_i\lambda_j\lambda_k\rangle$, the fifth $\langle\lambda_i\lambda_j\lambda_k\lambda_l\lambda_m\rangle$, etc. are found to be zero

[2] Here we use the common terminology in physics and refer to this pdf as a "multivariate Gaussian". It is called a "multivariate normal" distribution in statistics. Note that it is possible to generalize this definition to the case where C is only a positive semi-definite Hermitian matrix, using the notion of characteristic function (see appendix A).

by symmetry of the Gaussian pdf. The higher-order even ones (e.g. the fourth, the sixth, etc.) can be evaluated through the application of Wick's theorem, an elegant method of reducing high-order statistics to a combinatorics problem.

Wick's theorem states that high-order even moments of a grf are computed by connecting up all possible pairs of the field (Wick contractions) and writing down the covariance matrix for each pair using equation (1.16). For instance,

$$\begin{aligned} \langle\lambda_i\lambda_j\lambda_k\lambda_l\rangle &= \langle\lambda_i\lambda_j\rangle\langle\lambda_k\lambda_l\rangle + \langle\lambda_i\lambda_k\rangle\langle\lambda_j\lambda_l\rangle + \langle\lambda_i\lambda_l\rangle\langle\lambda_j\lambda_k\rangle \\ &= C_{ij}C_{kl} + C_{ik}C_{jl} + C_{il}C_{jk}. \end{aligned} \tag{1.17}$$

The number of terms generated in this fashion for the n-th order moment is $\prod_{i=1}^{n/2}(2i-1)$.

1.2.3.3 Marginals and conditionals of Gaussian random fields

Let us the split the grf up into two parts $x = [\![1, m]\!]$ and $y = [\![m+1, n]\!]$ $(m < n)$, so that

$$\lambda = \begin{pmatrix} \lambda_x \\ \lambda_y \end{pmatrix}, \quad \mu = \begin{pmatrix} \mu_x \\ \mu_y \end{pmatrix} \quad \text{and} \quad C = \begin{pmatrix} C_{xx} & C_{xy} \\ C_{yx} & C_{yy} \end{pmatrix}. \tag{1.18}$$

$C_{xy} = (C_{yx})^*$ since C is Hermitian.

Easy computation of marginal and conditional pdfs is a very convenient property of grfs. First of all, marginal and conditional densities of grfs are multivariate Gaussians. Therefore, all we need to calculate are their means and covariances. For the marginal pdfs, the results are

$$\langle\lambda_x\rangle = \mu_x, \tag{1.19}$$
$$\langle(\lambda_x-\mu_x)^*(\lambda_x-\mu_x)\rangle = C_{xx}, \tag{1.20}$$
$$\langle\lambda_y\rangle = \mu_y, \tag{1.21}$$
$$\langle(\lambda_y-\mu_y)^*(\lambda_y-\mu_y)\rangle = C_{yy}. \tag{1.22}$$

These expressions simply mean that the marginal means and marginal covariances are just the corresponding parts of the joint mean and covariance, as defined by equation (1.18).

Less trivially, here are the parameters of the conditional densities:

$$\mu_{x|y} \equiv \langle\lambda_x|\lambda_y\rangle = \mu_x + C_{xy}C_{yy}^{-1}(\lambda_y-\mu_y), \tag{1.23}$$
$$C_{x|y} \equiv \langle(\lambda_x-\mu_x)^*(\lambda_x-\mu_x)|\lambda_y\rangle = C_{xx} - C_{xy}C_{yy}^{-1}C_{yx}, \tag{1.24}$$
$$\mu_{y|x} \equiv \langle\lambda_y|\lambda_x\rangle = \mu_y + C_{yx}C_{xx}^{-1}(x-\mu_x), \tag{1.25}$$
$$C_{y|x} \equiv \langle(\lambda_y-\mu_y)^*(\lambda_y-\mu_y)|\lambda_x\rangle = C_{yy} - C_{yx}C_{xx}^{-1}C_{xy}. \tag{1.26}$$

A demonstration of these formulae can be found in appendix A. From these expressions, it is easy to see that for grfs, lack of covariance ($C_{xy} = 0$) implies independence, i.e. $\mathcal{P}(x,y) = \mathcal{P}(x)\mathcal{P}(y)$. This is most certainly not the case for general random fields. Similarly, if $\lambda_1, ..., \lambda_n$ are jointly Gaussian, then each λ_i is Gaussian-distributed, but not conversely.

A particular case is the optimal de-noising of a data set d, modeled as the sum of some signal s and a stochastic noise contribution n: $d = s+n$. We model all three fields d, s, n as grfs. Assuming a vanishing signal mean, an unbiased measurement (i.e. $\mu_d = \mu_s = \mu_n = 0$), and lack of covariance between signal and noise (i.e. $C_{sn} = C_{ns} = 0$, which implies $C_{sd} = C_{ss}$ and $C_{dd} = C_{ss} + C_{nn}$), equations (1.23) and (1.24) yield the famous Wiener filter equations:

$$\mu_{s|d} = C_{ss}\left(C_{ss}+C_{nn}\right)^{-1}d, \tag{1.27}$$
$$C_{s|d} = C_{ss} - C_{ss}\left(C_{ss}+C_{nn}\right)^{-1}C_{ss} = \left(C_{nn}^{-1}+C_{ss}^{-1}\right)^{-1}. \tag{1.28}$$

1.2.3.4 Log-normal random fields

In the case where $\delta(\mathbf{x})$ is the density contrast, gravitational evolution will yield very high positive density contrast amplitudes. In order to prevent negative mass ($\delta(\mathbf{x}) < -1$) while preserving $\langle\delta(\mathbf{x})\rangle = 0$, the resultant pdf must be strongly skewed (e.g. Peacock, 1999). In the absence of an exact pdf for the density field in non-linear regimes, solution to dynamical equations, one can describe the statistical properties of the evolved matter distribution by phenomenological probability distributions. A common choice is the log-normal distribution, which approximates well the one-point behavior observed in galaxy observations and N-body simulations (e.g. Hubble, 1934; Peebles, 1980; Coles & Jones, 1991; Gaztañaga & Yokoyama, 1993; Colombi, 1994; Kayo, Taruya & Suto, 2001; Neyrinck, Szapudi & Szalay, 2009). This is the model adopted as a prior for the density field in the HADES algorithm (Jasche & Kitaura, 2010; Jasche & Wandelt, 2012, see also table 4.2). The assumption is that the log-density, $\ln(1+\delta)$, instead of the density contrast δ, obeys Gaussian statistics.

If λ is a n-dimensional vector having multivariate Gaussian distribution with mean μ and covariance matrix C, then ξ, defined by its components $\xi_i = \exp(\lambda_i)$, has a multivariate log-normal distribution given by

$$\mathcal{P}(\xi|\mu, C) = \frac{1}{\sqrt{|2\pi C|}} \exp\left(-\frac{1}{2}\sum_{i=1}^{n}\sum_{j=1}^{n} \left(\ln(\xi_i) - \mu_i\right)^* C_{ij}^{-1} \left(\ln(\xi_j) - \mu_j\right)\right) \prod_k \frac{1}{\xi_k}. \tag{1.29}$$

The mean of ξ is ν defined by

$$\nu_i \equiv \langle \xi_i \rangle = \exp\left(\mu_i + \frac{1}{2}C_{ii}\right), \tag{1.30}$$

and its covariance matrix is D defined by

$$D_{ij} \equiv \langle (\xi_i - \mu_i)^* (\xi_j - \mu_j) \rangle = \exp\left(\mu_i + \mu_j + \frac{1}{2}(C_{ii} + C_{jj})\right) \left(\exp(C_{ij}) - 1\right). \tag{1.31}$$

In cosmology, we assume that $\lambda = \ln(1+\delta)$ is a grf with mean μ and covariance matrix C. Then $\delta = \exp(\lambda) - 1$ follows a log-normal distribution, given by

$$\mathcal{P}(\delta|\mu, C) = \frac{1}{\sqrt{|2\pi C|}} \exp\left(-\frac{1}{2}\sum_{i=1}^{n}\sum_{j=1}^{n} \left(\ln(1+\delta_i) - \mu_i\right)^* C_{ij}^{-1} \left(\ln(1+\delta_j) - \mu_j\right)\right) \prod_k \frac{1}{1+\delta_k}. \tag{1.32}$$

To ensure that $\langle \delta \rangle$ vanishes everywhere, i.e. that

$$\nu_i = \langle 1 + \delta_i \rangle = \exp\left(\mu_i + \frac{1}{2}C_{ii}\right) = 1, \tag{1.33}$$

one has to impose the following choice for μ:

$$\mu_i = -\frac{1}{2}C_{ii} = -\frac{1}{2}C_{00} = \mu_0. \tag{1.34}$$

We have used that $C_{ii} = C_{00}$, since the correlation function depends only on distance (assuming statistical homogeneity and isotropy). Hence, the mean for the lognormal distribution is the same throughout the entire field.

For further discussion on the log-normal behavior of density fields, see chapters 2 and 6.

1.2.4 Correlation functions and power spectra

1.2.4.1 Two-point correlation function and power spectrum

Definitions. The two-point correlation function is defined in configuration space as the joint ensemble average of the field at two different locations:

$$\xi(r) = \langle \lambda^*(\mathbf{x}) \lambda(\mathbf{x} + \mathbf{r}) \rangle. \tag{1.35}$$

It depends only on the norm of $\mathbf{r}$ if statistical isotropy and homogeneity hold.

The scalar field $\lambda(\mathbf{x})$ is usually written in terms of its Fourier components,

$$\lambda(\mathbf{x}) = \frac{1}{(2\pi)^{3/2}} \int \lambda(\mathbf{k}) \exp(\mathrm{i}\mathbf{k}\cdot\mathbf{x})\, \mathrm{d}^3\mathbf{k}, \tag{1.36}$$

or, equivalently,

$$\lambda(\mathbf{k}) = \frac{1}{(2\pi)^{3/2}} \int \lambda(\mathbf{x}) \exp(-\mathrm{i}\mathbf{k}\cdot\mathbf{x})\, \mathrm{d}^3\mathbf{x}. \tag{1.37}$$

The quantities $\lambda(\mathbf{k})$ are complex random variables. If $\lambda(\mathbf{x})$ is real, one has $\lambda(-\mathbf{k}) = \lambda^*(\mathbf{k})$ which means that half of the Fourier space contains redundant information.

The computation of the two-point correlator for $\lambda(\mathbf{k})$ in Fourier space gives:

$$\begin{aligned}
\left\langle \lambda^*(\mathbf{k})\lambda(\mathbf{k}')\right\rangle &= \frac{1}{(2\pi)^{3/2}}\frac{1}{(2\pi)^{3/2}}\iint \langle\lambda^*(\mathbf{x})\lambda(\mathbf{x}+\mathbf{r})\rangle \exp(\mathrm{i}(\mathbf{k}-\mathbf{k}')\cdot\mathbf{x} - \mathrm{i}\mathbf{k}'\cdot\mathbf{r})\,\mathrm{d}^3\mathbf{x}\,\mathrm{d}^3\mathbf{r} && (1.38)\\
&= \frac{1}{(2\pi)^3}\iint \xi(r)\exp(\mathrm{i}(\mathbf{k}-\mathbf{k}')\cdot\mathbf{x} - \mathrm{i}\mathbf{k}'\cdot\mathbf{r})\,\mathrm{d}^3\mathbf{x}\,\mathrm{d}^3\mathbf{r} && (1.39)\\
&= \frac{1}{(2\pi)^3}\,\delta_\mathrm{D}(\mathbf{k}-\mathbf{k}')\int \xi(r)\exp(\mathrm{i}\mathbf{k}\cdot\mathbf{r})\,\mathrm{d}^3\mathbf{r} && (1.40)\\
&\equiv \frac{1}{(2\pi)^{3/2}}\,\delta_\mathrm{D}(\mathbf{k}-\mathbf{k}')\,P(k), && (1.41)
\end{aligned}$$

where δ_D is a Dirac delta distribution and

$$P(k) \equiv \frac{1}{(2\pi)^{3/2}}\int \xi(r)\exp(\mathrm{i}\mathbf{k}\cdot\mathbf{r})\,\mathrm{d}^3\mathbf{r} \tag{1.42}$$

is defined to be the *power spectrum* of the field $\lambda(\mathbf{x})$ (this relation is known as the Wiener-Khinchin theorem). Because of statistical homogeneity and isotropy, it depends only on the norm of $\mathbf{k}$. The inverse relation between the two-point correlation function, $\xi(r)$, and the power spectrum, $P(k)$, reads

$$\xi(r) = \frac{1}{(2\pi)^{3/2}}\int P(k)\exp(-\mathrm{i}\mathbf{k}\cdot\mathbf{r})\,\mathrm{d}^3\mathbf{k}. \tag{1.43}$$

In spherical coordinates, using

$$\int_\Omega \exp\left(-\mathrm{i}kr\cos\theta\right)\mathrm{d}\Omega = \int_{\theta=0}^{\pi}\int_{\varphi=0}^{2\pi}\exp\left(-\mathrm{i}kr\cos\theta\right)\sin\theta\,\mathrm{d}\theta\,\mathrm{d}\varphi = 4\pi\frac{\sin(kr)}{kr}, \tag{1.44}$$

we obtain the one-dimensional relations between $\xi(r)$ and $P(k)$,

$$\begin{aligned}
P(k) &= \frac{2}{\sqrt{\pi}}\int_0^\infty \xi(r)\,j_0(kr)\,r^2\,\mathrm{d}r, && (1.45)\\
\xi(r) &= \frac{2}{\sqrt{\pi}}\int_0^\infty P(k)\,j_0(kr)\,k^2\,\mathrm{d}k, && (1.46)
\end{aligned}$$

where j_0 is the zero-th order spherical Bessel function,

$$j_0(x) \equiv \frac{\sin(x)}{x}. \tag{1.47}$$

Two-point probability function and two-point correlation function. The following physical interpretation of the two-point correlation function establishes a link between the ensemble average and the sample average. Indeed, correlation functions are directly related to multivariate probability functions (in fact, they are sometimes defined from them). Here we exemplify this fact for the density contrast at position $\mathbf{x}$, $\delta(\mathbf{x}) \equiv \rho(\mathbf{x})/\bar{\rho} - 1$.

Let us consider two infinitesimal volumes $\mathrm{d}V_1$ and $\mathrm{d}V_2$ inside the volume V. Let n_1 and n_2 be the particle densities at locations $\mathbf{x}_1$ and $\mathbf{x}_2$ and $n \equiv N/V$ the average numerical density. Then the density contrasts are $\delta(\mathbf{x}_1) = n_1/(n\,\mathrm{d}V_1) - 1$ and $\delta(\mathbf{x}_2) = n_2/(n\,\mathrm{d}V_2) - 1$ and the two-point correlation function reads

$$\xi(x_{12}) = \langle\delta(\mathbf{x}_1)\delta(\mathbf{x}_2)\rangle = \frac{\mathrm{d}N_{12}}{n^2\,\mathrm{d}V_1\,\mathrm{d}V_2} - 1, \tag{1.48}$$

where $x_{12} \equiv |\mathbf{x}_2 - \mathbf{x}_1|$ and $\mathrm{d}N_{12} = \langle n_1 n_2\rangle$ is the average number of *pairs* in the volumes $\mathrm{d}V_1$ and $\mathrm{d}V_2$ (i.e. the product of the number of particles in one volume times the number in the other volume). One can then rewrite

$$\mathrm{d}N_{12} = \langle n_1 n_2\rangle = n^2\left(1 + \xi(x_{12})\right)\mathrm{d}V_1\,\mathrm{d}V_2. \tag{1.49}$$

The physical interpretation of the two-point correlation function is that it measures the excess over uniform probability that two particles at volume elements $\mathrm{d}V_1$ and $\mathrm{d}V_2$ are separated by a distance x_{12}. If particle positions are drawn from uniform distributions (i.e. if there is no clustering), then $\mathrm{d}N_{12}$ is independent of the separation. In this case, the average number of pairs is the product of the average number of particles in the two volumes, $\langle n_1 n_2 \rangle = \langle n_1 \rangle \langle n_2 \rangle = n^2 \, \mathrm{d}V_1 \, \mathrm{d}V_2$ and the correlation ξ vanishes. Particles are said to be uncorrelated. Conversely, if ξ is non-zero, particle distributions are said to be correlated (if $\xi > 0$) or anti-correlated (if $\xi < 0$).

It is sometimes easier to derive the correlation function as the average density of particles at a distance r from another particle, i.e. by choosing the volume element $\mathrm{d}V_1$ such as $n \, \mathrm{d}V_1 = 1$. Then the number of pairs is given by the number of particles in volume $\mathrm{d}V_2$:

$$\mathrm{d}N_2 = n \, (1 + \xi(r)) \, \mathrm{d}V_2. \tag{1.50}$$

Hence, one can evaluate the correlation function as follows:

$$\xi(r) = \frac{\mathrm{d}N(r)}{n \, \mathrm{d}V} - 1 = \frac{\langle n(r) \rangle}{n} - 1, \tag{1.51}$$

i.e. as the average number of particles at distance r from any given particle, divided by the expected number of particles at the same distance in a uniform distribution, minus one. As $\mathrm{d}N_2$ is linked to the conditional probability that there is a particle in $\mathrm{d}V_2$ given that there is one in $\mathrm{d}V_1$, the previous expression is sometimes referred to as the *conditional density contrast*.

Two-point correlation function and power spectrum of Gaussian fields. If $\lambda(\mathbf{x})$ is a real grf of mean 0 and covariance matrix C, then equation (1.16) means that its two-point correlation function in configuration space is directly given by the covariance matrix: $\langle \lambda(\mathbf{x}_i) \lambda(\mathbf{x}_j) \rangle = C_{ij}$.

Additionally, if $\lambda(\mathbf{x})$ is also statistically homogeneous, equation (1.41) implies that $\lambda(\mathbf{k})$ has independent Fourier modes and that its covariance matrix in Fourier space is diagonal and contains the power spectrum coefficients $P(k)/(2\pi)^{3/2}$. Finally, according to Wick's theorem (section 1.2.3.2), one can write for any integer p:

$$\langle \lambda(\mathbf{k}_1) \ldots \lambda(\mathbf{k}_{2p+1}) \rangle = 0, \tag{1.52}$$

$$\begin{aligned} \langle \lambda(\mathbf{k}_1) \ldots \lambda(\mathbf{k}_{2p}) \rangle &= \sum_{\text{all pair associations}} \; \prod_{p \text{ pairs } (i,j)} \langle \lambda(\mathbf{k}_i) \lambda(\mathbf{k}_j) \rangle \\ &= \sum_{\text{all pair associations}} \; \prod_{p \text{ pairs } (i,j)} \delta_\mathrm{D}(\mathbf{k}_i - \mathbf{k}_j) \frac{P(k_i)}{(2\pi)^{3/2}}. \end{aligned} \tag{1.53}$$

Hence, for grfs, all statistical properties are included in two-point correlations. More specifically, all statistical properties of random variables $\lambda(\mathbf{k})$ are conclusively determined by the shape of the power spectrum $P(k)$.

1.2.4.2 Higher-order correlation functions

Higher-order correlation functions in configuration space. It is possible to define higher-order correlation functions, as the *connected part* (denoted by a subscript c) of the joint ensemble average of the field $\lambda(\mathbf{x})$ in an arbitrary number of locations. This can be formally written as

$$\begin{aligned} \xi_n(\mathbf{x}_1, \mathbf{x}_2, \ldots, \mathbf{x}_n) &= \langle \lambda(\mathbf{x}_1) \lambda(\mathbf{x}_2) \ldots \lambda(\mathbf{x}_n) \rangle_\mathrm{c} \\ &\equiv \langle \lambda(\mathbf{x}_1) \lambda(\mathbf{x}_2) \ldots \lambda(\mathbf{x}_n) \rangle - \sum_{\mathcal{S} \in \mathcal{P}(\{\mathbf{x}_1, \mathbf{x}_2, \ldots, \mathbf{x}_n\})} \; \prod_{s_i \in \mathcal{S}} \xi_{\#s_i}(\mathbf{x}_{s_i(1)}, \mathbf{x}_{s_i(2)}, \ldots, \mathbf{x}_{s_i(\#s_i)}), \end{aligned} \tag{1.54}$$

where the sum is made over the proper partitions (any partition except the set itself) of $\{\mathbf{x}_1, \mathbf{x}_2, \ldots, \mathbf{x}_n\}$ and s_i is a subset of $\{\mathbf{x}_1, \mathbf{x}_2, \ldots, \mathbf{x}_n\}$ contained in partition $\mathcal{S}$. When the average of $\lambda(\mathbf{x})$ is zero, only partitions that contain no singlets contribute. The decomposition in connected and non-connected parts of the joint ensemble average of the field can be easily visualized in a diagrammatic way (see e.g. Bernardeau *et al.*, 2002).

For grfs, as a consequence of Wick's theorem (section 1.2.3.2), all connected correlations functions are zero except ξ_2.

Higher-order correlators in Fourier space. This definition in configuration space can be extended to Fourier space. By statistical isotropy of the field, the n-th Fourier-space correlator does not depend on the direction of the $\mathbf{k}$-vectors. By statistical homogeneity, the $\mathbf{k}$-vectors have to sum up to zero. We can thus define $P_n(\mathbf{k}_1, \mathbf{k}_2, ..., \mathbf{k}_n)$ by

$$\langle \lambda(\mathbf{k}_1)\lambda(\mathbf{k}_2) \dots \lambda(\mathbf{k}_n) \rangle_\mathrm{c} \equiv \delta_\mathrm{D}(\mathbf{k}_1 + \mathbf{k}_2 + \dots + \mathbf{k}_n)\, P_n(\mathbf{k}_1, \mathbf{k}_2, ..., \mathbf{k}_n). \tag{1.55}$$

The Dirac delta distribution δ_D ensures that $\mathbf{k}$-vector configurations form closed polygons: $\sum_i \mathbf{k}_i = \mathbf{0}$.

Let us now examine the lowest-order connected moments.

Bispectrum. After the power spectrum, the second statistic of interest is the bispectrum B, for $n = 3$, defined by

$$\langle \lambda(\mathbf{k}_1)\lambda(\mathbf{k}_2)\lambda(\mathbf{k}_3) \rangle = \langle \lambda(\mathbf{k}_1)\lambda(\mathbf{k}_2)\lambda(\mathbf{k}_3) \rangle_\mathrm{c} \equiv \delta_\mathrm{D}(\mathbf{k}_1 + \mathbf{k}_2 + \mathbf{k}_3)\, B(\mathbf{k}_1, \mathbf{k}_2, \mathbf{k}_3). \tag{1.56}$$

Reduced bispectrum. It is convenient to define the reduced bispectrum $Q(\mathbf{k}_1, \mathbf{k}_2, \mathbf{k}_3)$ as

$$Q(\mathbf{k}_1, \mathbf{k}_2, \mathbf{k}_3) \equiv \frac{B(\mathbf{k}_1, \mathbf{k}_2, \mathbf{k}_3)}{P(k_1)P(k_2) + P(k_1)P(k_3) + P(k_2)P(k_3)}, \tag{1.57}$$

which takes away most of the dependence on scale and cosmology. The reduced bispectrum is useful for comparing different models, because its weak dependence on cosmology is known to break degeneracies between cosmological parameters and to isolate the effects of gravity (see Gil-Marín *et al.*, 2011, for an example).

Trispectrum. The trispectrum is the following correlator, for $n = 4$. It is defined as

$$\langle \lambda(\mathbf{k}_1)\lambda(\mathbf{k}_2)\lambda(\mathbf{k}_3)\lambda(\mathbf{k}_4) \rangle_\mathrm{c} \equiv \delta_\mathrm{D}(\mathbf{k}_1 + \mathbf{k}_2 + \mathbf{k}_3 + \mathbf{k}_4)\, T(\mathbf{k}_1, \mathbf{k}_2, \mathbf{k}_3, \mathbf{k}_4). \tag{1.58}$$

1.3 Dynamics of gravitational instability

The standard picture for the formation of the LSS as seen in galaxy surveys is the gravitational amplification of primordial density fluctuations. The dynamics of this process is mostly governed by gravitational interactions of collisionless (or at least, weakly-interacting) dark matter particles in an expanding universe.

For scales much smaller than the Hubble radius, relativistic effects (such as the curvature of the Universe or the apparent distance-redshift relation) are believed to be subdominant or negligible (e.g. Kolb & Turner, 1990, and references therein) and as we will show, the expansion of the background can be factored out by a redefinition of variables. Although the microscopic nature of dark matter particles remains unknown, candidates have to pass several tests in order to be viable (Taoso, Bertone & Masiero, 2008). In particular, particles which are relativistic at the time of structure formation lead to a large damping of small-scale fluctuations (Silk, 1968; Bond & Szalay, 1983), incompatible with observed structures. The standard theory thus requires dark matter particles to be cold during structure formation, i.e. non-relativistic well before the matter-dominated era (Peebles, 1982b; Blumenthal *et al.*, 1984; Davis *et al.*, 1985). For these two reasons, at scales much smaller than the Hubble radius the equations of motion can be well approximated by Newtonian gravity.

In addition, all dark matter particle candidates are extremely light compared to the mass of typical astrophysical objects such as stars or galaxies, with an expected number density of a least 10^{50} particles per Mpc^3. Therefore, discreteness effects are negligible and collisionless dark matter can be well described in the fluid limit approximation.

In this section, we present the dynamics of gravitational instability in the framework of Newtonian gravity within a flat, expanding background and in the fluid limit approximation. It is of course possible to do a detailed relativistic treatment of structure formation dynamics and cosmological perturbation theory (Bardeen, 1980; Mukhanov, Feldman & Brandenberger, 1992; Malik & Wands, 2009) and to derive the Newtonian limit from general relativity (see e.g. Peebles, 1980).

1.3.1 The Vlasov-Poisson system

The cosmological Poisson equation. Let us consider a large number of particles that interact only gravitationally in an expanding universe. For a particle of velocity $\mathbf{v}$ at position $\mathbf{r}$, the action of all other particles can be treated as a smooth gravitational potential induced by the local mass density $\rho(\mathbf{r})$,

$$\phi(\mathbf{r}) = \mathrm{G} \int \frac{\rho(\mathbf{r}' - \mathbf{r})}{|\mathbf{r}' - \mathbf{r}|} \, \mathrm{d}^3\mathbf{r}', \tag{1.59}$$

and the equation of motion reads

$$\frac{\mathrm{d}\mathbf{v}}{\mathrm{d}t} = -\nabla_{\mathbf{r}}\phi = \mathrm{G} \int \frac{\rho(\mathbf{r}' - \mathbf{r})\,(\mathbf{r}' - \mathbf{r})}{|\mathbf{r}' - \mathbf{r}|^3} \, \mathrm{d}^3\mathbf{r}'. \tag{1.60}$$

Examining gravitational instabilities in the context of an expanding universe requires to consider the departure from the homogeneous Hubble flow. It is natural to describe the positions of particles in terms of their comoving coordinates $\mathbf{x}$ such that the physical coordinates are $\mathbf{r} = a\mathbf{x}$ and of the conformal time τ, defined by $\mathrm{d}t = a(\tau)\,\mathrm{d}\tau$. Hereafter, when there is no ambiguity, we will denote $\nabla \equiv \nabla_{\mathbf{x}}$ and $\Delta \equiv \Delta_{\mathbf{x}}$. The Jacobian of the spatial coordinate transformation is $|J| = a^3$ so that the right-hand side of the previous equation becomes

$$\begin{aligned} \mathrm{G} \int \frac{\rho(\mathbf{r}' - \mathbf{r})\,(\mathbf{r}' - \mathbf{r})}{|\mathbf{r}' - \mathbf{r}|^3} \, \mathrm{d}^3\mathbf{r}' &= \mathrm{G} \int \frac{\rho(\mathbf{x}' - \mathbf{x})\,a\,(\mathbf{x}' - \mathbf{x})}{a^3|\mathbf{x}' - \mathbf{x}|^3} \, a^3\,\mathrm{d}^3\mathbf{x}' & (1.61)\\ &= \mathrm{G}a\bar{\rho} \int \frac{(\mathbf{x}' - \mathbf{x})}{|\mathbf{x}' - \mathbf{x}|^3} \, \mathrm{d}^3\mathbf{x}' + \mathrm{G}a\bar{\rho} \int \delta(\mathbf{x}' - \mathbf{x}) \frac{(\mathbf{x}' - \mathbf{x})}{|\mathbf{x}' - \mathbf{x}|^3} \, \mathrm{d}^3\mathbf{x}', & (1.62) \end{aligned}$$

where we have introduced the density contrast $\delta(\mathbf{x})$, defined as

$$\rho(\mathbf{x}, t) \equiv \bar{\rho}(t)\,[1 + \delta(\mathbf{x}, t)]\,, \tag{1.63}$$

where $\bar{\rho}(t) \propto 1/a^3$ (consequence of equation (1.3) with $w = 0$).

Velocities of particles are $\mathbf{v} = \dot{a}\mathbf{x} + a\,\mathrm{d}\mathbf{x}/\mathrm{d}t$, permitting us to define peculiar velocities as the difference between total velocities and the Hubble flow:

$$\mathbf{u} \equiv a\,\frac{\mathrm{d}\mathbf{x}}{\mathrm{d}t} = \mathbf{v} - \dot{a}\mathbf{x}. \tag{1.64}$$

$\mathrm{d}\mathbf{v}/\mathrm{d}t$ is written in terms of $\mathbf{u}$ as

$$\begin{aligned} \frac{\mathrm{d}\mathbf{v}}{\mathrm{d}t} &= \frac{\mathrm{d}\mathbf{u}}{\mathrm{d}t} + \ddot{a}\mathbf{x} + \dot{a}\,\frac{\mathrm{d}\mathbf{x}}{\mathrm{d}t} & (1.65)\\ &= \frac{\mathrm{d}\mathbf{u}}{\mathrm{d}t} + \ddot{a}\mathbf{x} + \frac{\dot{a}}{a}\,\mathbf{u}. & (1.66) \end{aligned}$$

By the use of the second Friedmann equation for the homogeneous background (equation (1.2)),

$$\ddot{a} = -\frac{4\pi\mathrm{G}}{3} a\bar{\rho}, \tag{1.67}$$

and Gauss's theorem,

$$\frac{4\pi}{3}\mathbf{x} = -\int \frac{(\mathbf{x}' - \mathbf{x})}{|\mathbf{x}' - \mathbf{x}|^3} \mathrm{d}^3\mathbf{x}', \tag{1.68}$$

the term $\ddot{a}\mathbf{x}$ is equal to

$$\mathrm{G}a\bar{\rho} \int \frac{(\mathbf{x}' - \mathbf{x})}{|\mathbf{x}' - \mathbf{x}|^3} \, \mathrm{d}^3\mathbf{x}' \equiv -\frac{1}{a}\nabla_{\mathbf{x}}\boldsymbol{\phi}, \tag{1.69}$$

which leaves for the peculiar velocity the following equation of motion (see equations (1.60), (1.62) and (1.66)):

$$\frac{\mathrm{d}\mathbf{u}}{\mathrm{d}t} + \frac{\dot{a}}{a}\,\mathbf{u} = \mathrm{G}a\bar{\rho} \int \delta(\mathbf{x}' - \mathbf{x}) \frac{(\mathbf{x}' - \mathbf{x})}{|\mathbf{x}' - \mathbf{x}|^3} \, \mathrm{d}^3\mathbf{x}' \equiv -\frac{1}{a}\nabla_{\mathbf{x}}\Phi. \tag{1.70}$$

Here we have defined the cosmological gravitational potential Φ such that $\phi \equiv \boldsymbol{\phi} + \Phi$ with, for the background,

$$\boldsymbol{\phi}(\mathbf{x}) = \frac{4\pi\mathrm{G}}{3} a^2\bar{\rho}\left(\frac{1}{2}|\mathbf{x}|^2\right) = -\mathcal{H}'\left(\frac{1}{2}|\mathbf{x}|^2\right), \quad \text{satisfying} \quad \Delta\boldsymbol{\phi} = 4\pi\mathrm{G}a^2\bar{\rho}. \tag{1.71}$$

Using the overall Poisson equation, $\Delta_{\mathbf{r}}\phi = \Delta\phi/a^2 = 4\pi G\bar{\rho}(1+\delta)$, we find that Φ follows a cosmological Poisson equation sourced only by density fluctuations, as expected:

$$\Delta\Phi = 4\pi G a^2 \bar{\rho}\delta = \frac{3}{2}\Omega_{\mathrm{m}}(\tau)\mathcal{H}^2(\tau)\delta. \tag{1.72}$$

The second equality comes from the first Friedmann equation in a flat universe (equation (1.1) with $k = 0$).

The Vlasov equation. Looking at equation (1.70), the momentum of a single particle of mass m is identified as:

$$\mathbf{p} = ma\mathbf{u}, \tag{1.73}$$

and the equation of motion reads:

$$\frac{\mathrm{d}\mathbf{p}}{\mathrm{d}t} = -m\nabla_{\mathbf{x}}\Phi = -ma\nabla_{\mathbf{r}}\Phi \quad \text{or} \quad \frac{\mathrm{d}\mathbf{p}}{\mathrm{d}\tau} = -ma\nabla_{\mathbf{x}}\Phi. \tag{1.74}$$

Let us now define the particle number density in phase space by $f(\mathbf{x}, \mathbf{p}, \tau)$. Phase-space conservation and Liouville's theorem imply the Vlasov equation (collisionless version of the Boltzmann equation):

$$\frac{\mathrm{d}f}{\mathrm{d}\tau} = \frac{\partial f}{\partial \tau} + \frac{\mathbf{p}}{ma}\cdot\nabla f - ma\nabla\Phi\cdot\frac{\partial f}{\partial \mathbf{p}} = 0. \tag{1.75}$$

Given equations (1.72) and (1.75), the Vlasov-Poisson system is closed.

1.3.2 Fluid dynamics approach, evolution equations in phase space

The Vlasov equation is very difficult to solve, since it is a partial differential equation involving seven variables, with non-linearity induced by the dependence of the potential Φ on the density through the Poisson equation. Its complicated structure prevents the analytic analysis of dark matter dynamics. In practice, we are usually not interested in solving the full phase-space dynamics, but only the evolution of the spatial distribution. It is therefore convenient to take momentum moments of the distribution function. This yields a fluid dynamics approach for the motion of collisionless dark matter. The zeroth-order momentum, by construction, relates the phase-space density to the density field,

$$\int f(\mathbf{x}, \mathbf{p}, \tau)\,\mathrm{d}^3\mathbf{p} \equiv \rho(\mathbf{x}, \tau). \tag{1.76}$$

The next order moments,

$$\int \frac{\mathbf{p}}{ma} f(\mathbf{x}, \mathbf{p}, \tau)\,\mathrm{d}^3\mathbf{p} \equiv \rho(\mathbf{x}, \tau)\mathbf{u}(\mathbf{x}, \tau), \tag{1.77}$$

$$\int \frac{\mathbf{p}_i\mathbf{p}_j}{m^2a^2} f(\mathbf{x}, \mathbf{p}, \tau)\,\mathrm{d}^3\mathbf{p} \equiv \rho(\mathbf{x}, \tau)\mathbf{u}_i(\mathbf{x}, \tau)\mathbf{u}_j(\mathbf{x}, \tau) + \sigma_{ij}(\mathbf{x}, \tau), \tag{1.78}$$

define the *peculiar velocity flow* $\mathbf{u}(\mathbf{x}, \tau)$ (average local velocity of particles in a region of space; for simplification, we use the same notation as the peculiar velocity of a single particle) and the *stress tensor* $\sigma_{ij}(\mathbf{x}, \tau)$ which can be related to the *velocity dispersion tensor*, $v_{ij}(\mathbf{x}, \tau)$, by $\sigma_{ij}(\mathbf{x}, \tau) \equiv \rho(\mathbf{x}, \tau)v_{ij}(\mathbf{x}, \tau)$.

By taking successive momentum moments of the Vlasov equation and integrating out phase-space information, a hierarchy of equations that couple successive moments of the distribution function can be constructed. The zeroth moment of the Vlasov equation gives the continuity equation,

$$\frac{\partial\delta(\mathbf{x}, \tau)}{\partial\tau} + \nabla\cdot\{[1 + \delta(\mathbf{x}, \tau)]\,\mathbf{u}(\mathbf{x}, \tau)\} = 0, \tag{1.79}$$

which describes the conservation of mass. Taking the first moment and subtracting $\bar{\rho}\,\mathbf{u}(\mathbf{x}, \tau)$ times the continuity equation yields the Euler equation,

$$\frac{\partial\mathbf{u}_i(\mathbf{x}, \tau)}{\partial\tau} + \mathcal{H}(\tau)\mathbf{u}_i(\mathbf{x}, \tau) + \mathbf{u}_j(\mathbf{x}, \tau)\cdot\nabla_j\mathbf{u}_i(\mathbf{x}, \tau) = -\nabla_i\Phi(\mathbf{x}, \tau) - \frac{1}{\rho(\mathbf{x}, \tau)}\nabla_j(\sigma_{ij}(\mathbf{x}, \tau)), \tag{1.80}$$

which describes the conservation of momentum. This equation is very similar to that of hydrodynamics, apart from an additional term which accounts for the expansion of the Universe and the fact that, contrary to perfect fluids, auto-gravitating systems may have an anisotropic stress tensor.

The infinite sequence of momentum moments of the Vlasov equation is usually truncated at this point and completed by fluid dynamics assumptions to close the system. Specifically, one postulates an Ansatz for the stress tensor, namely the equation of state of the cosmological fluid. For example, if the fluid is locally thermalized, the velocity dispersion becomes isotropic and proportional to the pressure (e.g. Bernardeau *et al.*, 2002):

$$\sigma_{ij} = -P\delta_{\mathrm{K}}^{ij}, \tag{1.81}$$

where δ_{K}^{ab} is a Kronecker symbol. Standard fluid dynamics also prescribes, with the addition of a viscous stress tensor, the following equation (e.g. Bernardeau *et al.*, 2002):

$$\sigma_{ij} = -P\delta_{\mathrm{K}}^{ij} + \zeta(\nabla \cdot \mathbf{u})\delta_{\mathrm{K}}^{ij} + \mu \left[\nabla_i \mathbf{u}_j + \nabla_j \mathbf{u}_i - \frac{2}{3}(\nabla \cdot \mathbf{u})\delta_{\mathrm{K}}^{ij}\right], \tag{1.82}$$

where ζ is the coefficient of bulk viscosity and μ is the coefficient of shear viscosity.

1.3.3 The single-stream approximation

At the early stages of cosmological gravitational instability, it is possible to further simplify and to rely on a different hypothesis, namely the *single-stream approximation*. At sufficiently large scales, gravity-induced cosmic flows will dominate over the velocity dispersion due to peculiar motions. The single-stream approximation consists in assuming that for CDM, velocity dispersion and pressure are negligible, i.e. $\sigma_{ij} = 0$, and that all particles have identical peculiar velocities. Hence, the density in phase space can be written

$$f(\mathbf{x}, \mathbf{p}, \tau) = \rho(\mathbf{x}, \tau)\, \delta_{\mathrm{D}}[\mathbf{p} - ma\mathbf{u}(\mathbf{x})] \,. \tag{1.83}$$

Note, that from its definition, equation (1.78), the stress tensor characterizes the deviation of particle motions from a single coherent flow.

The single-stream approximation only works at the beginning of gravitational structure formation, when structures had no time to collapse and virialize. Because of non-linearity in the Vlasov-Poisson system, later stages will involve the superposition of three or more streams in phase space, indicating the break down of the approximation at increasingly larger scales. The breakdown of $\sigma_{ij} \approx 0$, describing the generation of velocity dispersion or anisotropic stress due to the multiple-stream regime, is generically known as *shell-crossing*. Beyond that point, the density in phase space exhibits no simple form, generally preventing further analytic analysis. This issue will be discussed further in chapters 2 and 6.

The single-stream approximation yields the following system of equations:

$$\frac{\partial \delta(\mathbf{x}, \tau)}{\partial \tau} + \nabla \cdot \{[1 + \delta(\mathbf{x}, \tau)]\, \mathbf{u}(\mathbf{x}, \tau)\} = 0, \tag{1.84}$$

$$\frac{\partial \mathbf{u}_i(\mathbf{x}, \tau)}{\partial \tau} + \mathcal{H}(\tau)\mathbf{u}_i(\mathbf{x}, \tau) + \mathbf{u}_j(\mathbf{x}, \tau) \cdot \nabla_j \mathbf{u}_i(\mathbf{x}, \tau) = -\nabla_i \Phi(\mathbf{x}, \tau), \tag{1.85}$$

$$\Delta\Phi(\mathbf{x}, \tau) = 4\pi \mathrm{G} a^2(\tau)\bar{\rho}(\tau)\delta(\mathbf{x}, \tau). \tag{1.86}$$

It is a non-linear, closed system of equations involving the local density contrast, the local velocity field and the local gravitational potential.

There exists no general analytic solution to the fluid dynamics of collisionless self-gravitating CDM, even in the single-stream regime. However, literature provides several different analytic perturbative expansion techniques to yield approximate solutions for the dark matter dynamics, which we briefly review below (sections 1.4 and 1.5).

1.4 Eulerian perturbation theory

1.4.1 Eulerian linear perturbation theory

As mentioned above, at large scales and during the early stages of gravitational evolution, we expect the matter distribution to be smooth and to follow a single velocity stream. In this regime, it is therefore possible to linearize equation (1.84) and (1.85), assuming that fluctuations of density are small compared to the homogeneous contribution and that gradients of velocity fields are small compared to the Hubble parameter,

$$|\delta(\mathbf{x},\tau)| \ll 1, \tag{1.87}$$
$$|\nabla_j \mathbf{u}_i(\mathbf{x},\tau)| \ll \mathcal{H}(\tau). \tag{1.88}$$

We obtain the equation of motion in the *linear regime*,

$$\frac{\partial\delta(\mathbf{x},\tau)}{\partial\tau} + \theta(\mathbf{x},\tau) = 0, \tag{1.89}$$
$$\frac{\partial\mathbf{u}(\mathbf{x},\tau)}{\partial\tau} + \mathcal{H}(\tau)\mathbf{u}(\mathbf{x},\tau) = -\nabla\Phi(\mathbf{x},\tau), \tag{1.90}$$

where $\theta(\mathbf{x},\tau) \equiv \nabla\cdot\mathbf{u}(\mathbf{x},\tau)$ is the divergence of the velocity field. The velocity field, as any vector field, is completely described by its divergence $\theta(\mathbf{x},\tau)$ and its curl, referred to as the vorticity, $\mathbf{w}(\mathbf{x},\tau) \equiv \nabla\times\mathbf{u}(\mathbf{x},\tau)$, whose equations of motion follow from taking the divergence and the curl of equation (1.85) and using the Poisson equation:

$$\frac{\partial\theta(\mathbf{x},\tau)}{\partial\tau} + \mathcal{H}(\tau)\theta(\mathbf{x},\tau) + 4\pi\mathrm{G}a^2(\tau)\bar{\rho}(\tau)\delta(\mathbf{x},\tau) = 0, \tag{1.91}$$
$$\frac{\partial\mathbf{w}(\mathbf{x},\tau)}{\partial\tau} + \mathcal{H}(\tau)\mathbf{w}(\mathbf{x},\tau) = 0. \tag{1.92}$$

Since vorticity is not sourced in the linear regime, any initial vorticity rapidly decays due to the expansion of the Universe. Indeed, its evolution immediately follows from equation (1.92): $\mathbf{w}(\tau) \propto 1/a(\tau)$. In the non-linear regime, the emergence of anisotropic stress in the right-hand side of Euler's equation can lead to vorticity generation (Pichon & Bernardeau, 1999).

The density contrast evolution follows by replacing equation (1.89) and its time derivative in equation (1.91):

$$\frac{\partial^2\delta(\mathbf{x},\tau)}{\partial\tau^2} + \mathcal{H}(\tau)\frac{\partial\delta(\mathbf{x},\tau)}{\partial\tau} = 4\pi\mathrm{G}a^2(\tau)\bar{\rho}(\tau)\delta(\mathbf{x},\tau) = \frac{3}{2}\Omega_\mathrm{m}(\tau)\mathcal{H}^2(\tau)\delta(\mathbf{x},\tau). \tag{1.93}$$

1.4.2 The growth of fluctuations in linear theory

This linear equation allows us to look for different fluctuation modes, decoupling spatial and time contributions by writing $\delta(\mathbf{x},\tau) = D_1(\tau)\,\delta(\mathbf{x},0)$, where some "initial" reference time is labeled as 0 and where $D_1(\tau)$ is called the *linear growth factor*. The time dependence of the fluctuation growth rate satisfies

$$\frac{\mathrm{d}^2 D_1(\tau)}{\mathrm{d}\tau^2} + \mathcal{H}(\tau)\frac{\mathrm{d}D_1(\tau)}{\mathrm{d}\tau} = \frac{3}{2}\Omega_\mathrm{m}(\tau)\mathcal{H}^2(\tau)D_1(\tau), \tag{1.94}$$

regardless of $\mathbf{x}$ (or of the Fourier mode $\mathbf{k}$): in the linear regime, the growth of fluctuations is scale-independent. This equation, together with Friedmann's equations, equations (1.7) and (1.9), determines the growth of density perturbations in the linear regime as a function of cosmological parameters. There are two independent solutions, the fastest growing mode $D_1^{(+)}(\tau)$ and the slowest growing mode $D_1^{(-)}(\tau)$. The evolution of the density contrast is then given by:

$$\delta(\mathbf{x},\tau) = D_1^{(+)}(\tau)\delta_+(\mathbf{x}) + D_1^{(-)}(\tau)\delta_-(\mathbf{x}), \tag{1.95}$$

where $\delta_+(\mathbf{x})$ and $\delta_-(\mathbf{x})$ are two functions of position only describing the initial density field configuration.

In terms of the scale factor and using Friedmann's equations, equation (1.94) can be rewritten as

$$a^2\frac{\mathrm{d}^2 D_1}{\mathrm{d}a^2} + \left(\Omega_\Lambda(a) - \frac{\Omega_\mathrm{m}(a)}{2} + 2\right)a\frac{\mathrm{d}D_1}{\mathrm{d}a} = \frac{3}{2}\Omega_\mathrm{m}(a)D_1, \tag{1.96}$$

where the cosmological parameters $\Omega_\Lambda(a)$ and $\Omega_\mathrm{m}(a)$ now depend on the scale factor (for more details on this derivation and a generalization to time-varying dark energy models, see Percival, 2005b).

Using the linearized continuity equation, equation (1.89), the velocity divergence is given by

$$\theta(\mathbf{x},\tau) = -\mathcal{H}(\tau)\left[f(\Omega_i)\delta_+(\mathbf{x},\tau) + g(\Omega_i)\delta_-(\mathbf{x},\tau)\right]. \tag{1.97}$$

It does not depend directly on the linear growth factor of each mode, but on its logarithmic derivative, the exponent in the momentary power law relating D to a,

$$f(\Omega_i) \equiv \frac{1}{\mathcal{H}(\tau)}\frac{\mathrm{d}\ln D_1^{(+)}}{\mathrm{d}\tau} = \frac{\mathrm{d}\ln D_1^{(+)}}{\mathrm{d}\ln a}, \quad g(\Omega_i) \equiv \frac{1}{\mathcal{H}(\tau)}\frac{\mathrm{d}\ln D_1^{(-)}}{\mathrm{d}\tau} = \frac{\mathrm{d}\ln D_1^{(-)}}{\mathrm{d}\ln a}, \tag{1.98}$$

with $\delta_\pm(\mathbf{x},\tau) \equiv D_1^{(\pm)}(\tau)\delta_\pm(\mathbf{x})$.

We now review some cosmological models for which analytic expressions exist.

1. For a standard cold dark matter (SCDM) model, i.e. a particular case of an Einstein-de Sitter universe (Einstein & de Sitter, 1932) where dark matter is cold, the cosmological parameters are time-independent: $\Omega_\mathrm{m}(a) = 1$ and $\Omega_\Lambda(a) = 0$. Using equation (1.96), the evolution of the linear growth factor satisfies

$$a^2\frac{\mathrm{d}^2 D_1}{\mathrm{d}a^2} + \frac{3}{2}a\frac{\mathrm{d}D_1}{\mathrm{d}a} = \frac{3}{2}D_1. \tag{1.99}$$

   Two independent solutions are

$$D_1^{(+)} \propto a, \quad f(\Omega_\mathrm{m}=1,\Omega_\Lambda=0) = 1, \quad D_1^{(-)} \propto a^{-3/2}, \quad g(\Omega_\mathrm{m}=1,\Omega_\Lambda=0) = -\frac{3}{2}, \tag{1.100}$$

   thus density fluctuations grow as the scale factor, $\delta \propto a$, once the decaying mode has vanished.

2. For an open cold dark matter (OCDM) model, the cosmological parameters are $\Omega_\mathrm{m}(a) < 1$ and $\Omega_\Lambda(a) = 0$. The solutions of equation (1.96) are (Groth & Peebles, 1975), with $x \equiv a(\tau)(1/\Omega_\mathrm{m}^{(0)} - 1)$,

$$D_1^{(+)} = 1 + \frac{3}{x} + 3\,\frac{(1+x)^{1/2}}{x^{3/2}}\ln\left[(1+x)^{1/2} - x^{1/2}\right], \quad D_1^{(-)} = \frac{(1+x)^{1/2}}{x^{3/2}}. \tag{1.101}$$

   The dimensionless parameter g is calculated to be

$$g(\Omega_\mathrm{m},\Omega_\Lambda=0) = -\frac{\Omega_\mathrm{m}}{2} - 1, \tag{1.102}$$

   and the dimensionless parameter f can be approximated by (Peebles, 1976, 1980)

$$f(\Omega_\mathrm{m},\Omega_\Lambda=0) \approx \Omega_\mathrm{m}^{3/5}. \tag{1.103}$$

   As $\Omega_\mathrm{m} \to 0$ ($a \to \infty$ and $x \to \infty$), $D_1^{(+)} \to 1$ and $D_1^{(-)} \sim x^{-1}$: perturbations cease to grow.

3. For a universe with cold dark matter and a cosmological constant, $\Omega_\mathrm{m}(a) < 1$ and $0 < \Omega_\Lambda(a) \leq 1$ (ΛCDM model), allowing the possibility of a curvature term ($\Omega_\mathrm{tot}(a) = \Omega_\mathrm{m}(a) + \Omega_\Lambda(a) \neq 1$), the first Friedmann equation, equation (1.1), allows to write the Hubble parameter as

$$H(a) = H_0\sqrt{\Omega_\Lambda^{(0)} + (1 - \Omega_\Lambda^{(0)} - \Omega_\mathrm{m}^{(0)})a^{-2} + \Omega_\mathrm{m}^{(0)}a^{-3}}. \tag{1.104}$$

   It can be checked that this expression is a solution of equation (1.96). The decaying mode is then

$$D_1^{(-)} \propto H(a) = \frac{\mathcal{H}(a)}{a}. \tag{1.105}$$

   Using this particular solution and the variation of parameters method, the other solution is found to be (Heath, 1977; Carroll, Press & Turner, 1992; Bernardeau *et al.*, 2002)

$$D_1^{(+)} \propto a^3 H^3(a)\int_0^a \frac{\mathrm{d}\tilde{a}}{\tilde{a}^3 H^3(\tilde{a})}. \tag{1.106}$$

   Due to equations (1.7) and (1.105), one finds for arbitrary Ω_m and Ω_Λ,

$$g(\Omega_\mathrm{m},\Omega_\Lambda) = \Omega_\Lambda - \frac{\Omega_\mathrm{m}}{2} - 1, \tag{1.107}$$

and f can be approximated by (Lahav *et al.*, 1991)

$$f(\Omega_\mathrm{m}, \Omega_\Lambda) \approx \left[\frac{\Omega_\mathrm{m}^{(0)} a^{-3}}{\Omega_\mathrm{m}^{(0)} a^{-3} + (1 - \Omega_\Lambda^{(0)} - \Omega_\mathrm{m}^{(0)}) a^{-2} + \Omega_\Lambda^{(0)}} \right]^{3/5} \tag{1.108}$$

or (Lightman & Schechter, 1990; Carroll, Press & Turner, 1992)

$$f(\Omega_\mathrm{m}, \Omega_\Lambda) \approx \left[\frac{\Omega_\mathrm{m}^{(0)} a^{-3}}{\Omega_\mathrm{m}^{(0)} a^{-3} + (1 - \Omega_\Lambda^{(0)} - \Omega_\mathrm{m}^{(0)}) a^{-2} + \Omega_\Lambda^{(0)}} \right]^{4/7}. \tag{1.109}$$

For flat Universe, $\Omega_\mathrm{m} + \Omega_\Lambda = 1$, we have (Bouchet *et al.*, 1995; Bernardeau *et al.*, 2002)

$$f(\Omega_\mathrm{m}, \Omega_\Lambda = 1 - \Omega_\mathrm{m}) \approx \Omega_\mathrm{m}^{5/9}. \tag{1.110}$$

In the case of the Einstein-de Sitter universe, an interpretation of the growing and decaying modes can be easily given. Referring to the solution for the growth factor, equation (1.100), the initial density field (equation (1.95)) and the initial velocity field (equation (1.97)) are written

$$\begin{aligned} \delta_\mathrm{init}(\mathbf{x}) &\equiv \delta(\mathbf{x}, 0) = \delta_+(\mathbf{x}) + \delta_-(\mathbf{x}), & (1.111)\\ \theta_\mathrm{init}(\mathbf{x}) &\equiv \theta(\mathbf{x}, 0) = -\mathcal{H}(0) \left[\delta_+(\mathbf{x}) - \frac{3}{2}\delta_-(\mathbf{x}) \right], & (1.112) \end{aligned}$$

if we assume that D_+ and D_- are normalized to unity at the initial time. These relations can be inverted to give

$$\begin{aligned} \delta_+(\mathbf{x}) &= \frac{3}{5}\left(\delta_\mathrm{init}(\mathbf{x}) - \frac{2}{3}\frac{\theta_\mathrm{init}(\mathbf{x})}{\mathcal{H}(0)} \right), & (1.113)\\ \delta_-(\mathbf{x}) &= \frac{2}{5}\left(\delta_\mathrm{init}(\mathbf{x}) + \frac{\theta_\mathrm{init}(\mathbf{x})}{\mathcal{H}(0)} \right). & (1.114) \end{aligned}$$

From these expressions, the interpretation of the modes become clear. The sign is significant: recall that for a growing mode alone we would expect $\theta_\mathrm{init} = -\mathcal{H}(0)\delta_\mathrm{init}$ and for a decaying mode alone, $\theta_\mathrm{init} = 3/2\,\mathcal{H}(0)\delta_\mathrm{init}$. A pure growing mode corresponds to the case where the density and velocity fields are initially "in phase", in the sense that the velocity field converges towards the potential wells defined by the density field. A pure decaying mode corresponds to the case where the density and velocity fields are initially "opposite in phase", the velocity field being such that particles escape potential wells.

1.4.3 Eulerian perturbation theory at higher order

At higher order, Eulerian perturbation theory can be implemented by expanding the density and velocity fields,

$$\begin{aligned} \delta(\mathbf{x}, \tau) &= \sum_{n=1}^{\infty} \delta^{(n)}(\mathbf{x}, \tau) = \delta^{(1)}(\mathbf{x}, \tau) + \delta^{(2)}(\mathbf{x}, \tau) + \dots, & (1.115)\\ \theta(\mathbf{x}, \tau) &= \sum_{n=1}^{\infty} \theta^{(n)}(\mathbf{x}, \tau) = \theta^{(1)}(\mathbf{x}, \tau) + \theta^{(2)}(\mathbf{x}, \tau) + \dots, & (1.116) \end{aligned}$$

where $\delta^{(1)}(\mathbf{x}, \tau)$ and $\theta^{(1)}(\mathbf{x}, \tau)$ are the linear order solution studied in the previous section. Focusing only on the growing mode, the first-order density field reads,

$$\delta^{(1)}(\mathbf{x}, \tau) = D_1(\tau)\delta_\mathrm{init}(\mathbf{x}), \tag{1.117}$$

with $D_1(\tau) \equiv D_1^{(+)}(\tau)$ and $\delta_\mathrm{init}(\mathbf{x}) = \delta_+(\mathbf{x})$. $\delta^{(2)}(\mathbf{x}, \tau)$ describes to leading order the non-local evolution of the density field due to gravitational interactions. It is found to be proportional to the *second-order growth factor*, $D_2(\tau)$, which satisfies the differential equation (equation 43 in Bouchet *et al.*, 1995)

$$a^2 \frac{\mathrm{d}^2 D_2}{\mathrm{d}a^2} + \left(\Omega_\Lambda(a) - \frac{\Omega_\mathrm{m}(a)}{2} + 2 \right) a \frac{\mathrm{d}D_2}{\mathrm{d}a} = \frac{3}{2}\Omega_\mathrm{m}(a) \left[D_2 - (D_1^{(+)})^2 \right]. \tag{1.118}$$

In the codes implemented for this thesis, we use the fitting function

$$D_2(\tau) \approx -\frac{3}{7} D_1^2(\tau) \Omega_\mathrm{m}^{-1/143}, \tag{1.119}$$

valid for a flat ΛCDM model (Bouchet *et al.*, 1995). Depending on the cosmological parameters, different expressions can be found in the literature (see e.g. Bernardeau *et al.*, 2002), but $D_2(\tau)$ always stays of the order of $D_1^2(\tau)$ as expected in perturbation theory.

A detailed presentation of non-linear Eulerian perturbation theory involves new types of objects (kernels, propagators, vertices) and is beyond the scope of this thesis. For an existing review, see e.g. Bernardeau *et al.* (2002).

1.5 Lagrangian perturbation theory

1.5.1 Lagrangian fluid approach for cold dark matter

As we have seen (section 1.3.2), our approach is based on the assumption that CDM is well described by a fluid. A way of looking at fluid motion is to focus on specific locations in space through which the fluid flows as time passes. It is then possible to study dynamics of density and velocity fields in this context, which constitutes the Eulerian point of view. We have developed Eulerian perturbation theory in section 1.4.

Alternatively, in fluid dynamics, one can choose to describe the field by following the trajectories of particles or fluid elements. This is the so-called Lagrangian description. The goal of this paragraph is to apply this description to the cosmological fluid and to build *Lagrangian perturbation theory* in this framework.

Mapping from Lagrangian to Eulerian coordinates. In Lagrangian description, the object of interest is not the position of particles but the *displacement field* $\Psi(\mathbf{q})$ which maps the initial comoving particle position $\mathbf{q}$ into its final comoving Eulerian position $\mathbf{x}$, (e.g. Buchert, 1989; Bouchet *et al.*, 1995; Bernardeau *et al.*, 2002):

$$\mathbf{x}(\mathbf{q},\tau) \equiv \mathbf{q} + \mathbf{\Psi}(\mathbf{q},\tau). \tag{1.120}$$

Let $J(\mathbf{q},\tau)$ be the Jacobian of the transformation between Lagrangian and Eulerian coordinates,

$$J(\mathbf{q},\tau) \equiv \left| \frac{\partial \mathbf{x}}{\partial \mathbf{q}} \right| = |\det \mathcal{D}| = |\det(\mathcal{I} + \mathcal{R})| \,, \tag{1.121}$$

where the deformation tensor $\mathcal{D}$ can be written as the identity tensor $\mathcal{I}$ plus the shear of the displacement,[3] $\mathcal{R} \equiv \partial\mathbf{\Psi}/\partial\mathbf{q}$. The Jacobian can be obtained by requiring that the Lagrangian mass element be conserved in the relationship between density contrast and trajectories:

$$\rho(\mathbf{x},\tau)\,\mathrm{d}^3\mathbf{x} = \rho(\mathbf{q})\,\mathrm{d}^3\mathbf{q} \quad \Rightarrow \quad \bar{\rho}(\tau)\,[1+\delta(\mathbf{x},\tau)]\,\mathrm{d}^3\mathbf{x} = \bar{\rho}(\tau)\mathrm{d}^3\mathbf{q}, \tag{1.122}$$

Hence,

$$J(\mathbf{q},\tau) = \frac{1}{1+\delta(\mathbf{x},\tau)} \quad \text{or} \quad \delta(\mathbf{x},\tau) = J^{-1}(\mathbf{q},\tau) - 1. \tag{1.123}$$

Note that this result (without the absolute value for J) is valid as long as no shell-crossing occurs. At the first crossing of trajectories, fluid elements with different initial positions $\mathbf{q}$ end up at the same Eulerian position $\mathbf{x}$ through the mapping in equation (1.120). The Jacobian vanishes and one expects a singularity, namely a collapse to infinite density. At this point, the description of dynamics in terms of a mapping does not hold anymore, the correct description involves a summation over all possible streams.

Equation of motion in Lagrangian coordinates. The equation of motion for a fluid element, equation (1.70), reads in conformal time,

$$\frac{\partial \mathbf{u}}{\partial \tau} + \mathcal{H}(\tau)\mathbf{u} = -\nabla_\mathbf{x}\Phi, \tag{1.124}$$

[3] $\mathcal{R}$ is mathematically a tensor. It is sometimes referred to as the tidal tensor and noted $\mathcal{T}$. We will avoid this nomenclature and notation here, so as not to introduce confusion with the Hessian of the gravitational potential $\mathcal{T} \equiv \partial^2\Phi/\partial\mathbf{x}^2$ (see section C.2).

where Φ is the cosmological gravitational potential and $\nabla_{\mathbf{x}}$ is the gradient operator in Eulerian comoving coordinates $\mathbf{x}$. Taking the divergence of this equation, noting that $\mathbf{u} = \mathrm{d}\mathbf{x}/\mathrm{d}\tau = \partial\mathbf{\Psi}/\partial\tau$, using equation (1.123) and the Poisson equation, equation (1.72), and multiplying by the Jacobian, we obtain

$$J(\mathbf{q},\tau)\,\nabla_{\mathbf{x}} \cdot \left[\frac{\partial^2\mathbf{\Psi}}{\partial\tau^2} + \mathcal{H}(\tau)\frac{\partial\mathbf{\Psi}}{\partial\tau}\right] = \frac{3}{2}\Omega_\mathrm{m}(\tau)\mathcal{H}^2(\tau)\,[J(\mathbf{q},\tau)-1]\,. \tag{1.125}$$

This equation shows the principal difficulty of the Lagrangian approach: the gradient operator has to be taken with reference to the Eulerian variable $\mathbf{x}$, which depends on $\mathbf{q}$ according to equation (1.120). Equation (1.125) can be rewritten in terms of Lagrangian coordinates only by using $(\nabla_{\mathbf{x}})_i = \left[\delta_\mathrm{K}^{ij} + \mathbf{\Psi}_{i,j}\right]^{-1}(\nabla_{\mathbf{q}})_j$, where $\mathbf{\Psi}_{i,j} \equiv \partial\mathbf{\Psi}_i/\partial\mathbf{q}_j = \mathcal{R}_{ij}$ are the shears of the displacement. The resulting non-linear differential equation for $\mathbf{\Psi}(\mathbf{q},\tau)$ is then solved perturbatively, expanding about its linear solution.

1.5.2 The Zel'dovich approximation

Displacement field in the Zel'dovich approximation. In Lagrangian approach, non-linearities of the dynamics are encoded in the relation between $\mathbf{q}$ and $\mathbf{x}$ (equation (1.120)) and in the relation between the displacement field and the local density (equation (1.123)). The Zel'dovich approximation (Zel'dovich, 1970; Shandarin & Zel'dovich, 1989, hereafter ZA) is first order Lagrangian perturbation theory. It consists of taking the linear solution of equation (1.125) for the displacement field while keeping the general equation with the Jacobian, equation (1.123), to reconstruct the density field. At linear order in the displacement field, the relation between the gradients in Eulerian and Lagrangian coordinates is $J(\mathbf{q},\tau)\nabla_{\mathbf{x}} \approx \nabla_{\mathbf{q}}$, and the first-order Jacobian is $J(\mathbf{q},\tau) \approx 1 + \nabla_{\mathbf{q}}\cdot\mathbf{\Psi}$. The equation to solve becomes

$$\nabla_{\mathbf{q}} \cdot \left[\frac{\partial^2\mathbf{\Psi}}{\partial\tau^2} + \mathcal{H}(\tau)\frac{\partial\mathbf{\Psi}}{\partial\tau}\right] = \frac{3}{2}\Omega_\mathrm{m}(\tau)\mathcal{H}^2(\tau)\,(\nabla_{\mathbf{q}}\cdot\mathbf{\Psi})\,. \tag{1.126}$$

The addition of any divergence-free displacement field to a solution of the previous equation will also be a solution. In the following, we remove this indeterminacy by assuming that the movement is potential, i.e. $\nabla_{\mathbf{q}} \times \mathbf{\Psi} = 0$. Introducing the divergence of the Lagrangian displacement field, $\psi \equiv \nabla_{\mathbf{q}}\cdot\mathbf{\Psi}$, one has to solve,

$$\psi'' + \mathcal{H}(\tau)\psi' = \frac{3}{2}\Omega_\mathrm{m}(\tau)\mathcal{H}^2(\tau)\psi. \tag{1.127}$$

Therefore, the linear solution of equation (1.125) is separable into a product of a temporal and a spatial contribution. It can be written as $\mathbf{\Psi}^{(1)}(\mathbf{q},\tau)$ such that

$$\psi^{(1)}(\mathbf{q},\tau) \equiv \nabla_{\mathbf{q}}\cdot\mathbf{\Psi}^{(1)}(\mathbf{q},\tau) = -D_1(\tau)\,\delta(\mathbf{q}), \tag{1.128}$$

where $D_1(\tau)$ denotes the linear growth factor studied in section 1.4.1 and $\delta(\mathbf{q})$ describes the growing mode of the initial density contrast field in Lagrangian coordinates. This can be checked in equation (1.127) using the differential equation satisfied by the growth factor, equation (1.94). The above choice for the spatial contribution permits to recover the linear Eulerian behaviour, since initially $\delta(\mathbf{x}) \approx D_1(\tau)\delta(\mathbf{q}) \approx (1+\psi)^{-1} - 1 \approx -\psi$.

Note that the evolution of fluid elements at linear order is *local evolution*, i.e. it does not depend on the behavior of the rest of fluid elements. We have assumed that at linear order, the displacement field is entirely determined by its divergence, i.e. that vorticity vanishes. As we have already noted from equation (1.92), in the linear regime, any initial vorticity decays away due to the expansion of the Universe. Thus, one might consider that the solutions will apply anyway, even if vorticity is initially present, because at later times it will have negligible effect. Similarly, we have neglected the effect of the decaying mode in equation (1.95).

Shell-crossing in the Zel'dovich approximation. Since the displacement field in the ZA is curl-free, it is convenient to introduce the potential from which it derives, $\phi^{(1)}(\mathbf{q})$, such that $\mathbf{\Psi}^{(1)}(\mathbf{q},\tau) = -D_1(\tau)\nabla_{\mathbf{q}}\phi^{(1)}(\mathbf{q})$. At linear order in the displacement field, its shear $\mathcal{R} \equiv \partial\mathbf{\Psi}^{(1)}/\partial\mathbf{q}$ is equal to $-D_1(\tau)\mathrm{H}(\phi^{(1)}(\mathbf{q}))$. Let $\lambda_1(\mathbf{q}) \leq \lambda_2(\mathbf{q}) \leq \lambda_3(\mathbf{q})$ be the local eigenvalues of the Hessian of the Zel'dovich potential $\phi^{(1)}(\mathbf{q})$. At conformal time τ, these values have grown of a factor $-D_1(\tau)$ to give the eigenvalues of the shear of the displacement $\mathcal{R}$. Using equation (1.123), the density contrast may then be written as (e.g. Bouchet *et al.*, 1995; Bernardeau *et al.*, 2002)

$$1 + \delta(\mathbf{x},\tau) = \frac{1}{[1-\lambda_1(\mathbf{q})D_1(\tau)]\,[1-\lambda_2(\mathbf{q})D_1(\tau)]\,[1-\lambda_3(\mathbf{q})D_1(\tau)]}. \tag{1.129}$$

This equation allows an interpretation of what happens at shell-crossing in the ZA. If all eigenvalues λ_i are negative, this is a developing underdense region, eventually reaching $\delta = -1$. If λ_3 only is positive, when $\lambda_3 D_1(\tau) \to 1$, the ZA leads to a planar collapse to infinite density along the axis of λ_3 and the formation of a two-dimensional "cosmic pancake". In the case when two eigenvalues are positive, $\lambda_2, \lambda_3 > 0$, there is collapse to a filament. The case $\lambda_1, \lambda_2, \lambda_3 > 0$ leads to gravitational collapse along all directions (spherical collapse if $\lambda_1 \approx \lambda_2 \approx \lambda_3$). This picture of gravitational structure formation leads to a cosmic web classification algorithm, which labels different regions either as voids, sheets, filaments, or halos (see Hahn *et al.*, 2007a; Lavaux & Wandelt, 2010, and section C.2).

1.5.3 Second-order Lagrangian perturbation theory

Displacement field in second-order Lagrangian perturbation theory. The Zel'dovich approximation being local, it fails at sufficiently non-linear stages when particles are forming gravitationally bound structures instead of following straight lines. Already second-order Lagrangian perturbation theory (hereafter 2LPT) provides a remarkable improvement over the ZA in describing the global properties of density and velocity fields (Melott, Buchert & Weiß, 1995). The solution of equation (1.125) up to second order takes into account the fact that gravitational instability is *non-local*, i.e. it includes the correction to the ZA displacement due to gravitational tidal effects. It reads

$$\mathbf{x}(\tau) = \mathbf{q} + \mathbf{\Psi}(\mathbf{q},\tau) = \mathbf{q} + \mathbf{\Psi}^{(1)}(\mathbf{q},\tau) + \mathbf{\Psi}^{(2)}(\mathbf{q},\tau), \quad \text{or} \quad \mathbf{\Psi}(\mathbf{q},\tau) = \mathbf{\Psi}^{(1)}(\mathbf{q},\tau) + \mathbf{\Psi}^{(2)}(\mathbf{q},\tau), \tag{1.130}$$

where the divergence of the first order solution is the same as in the ZA (equation (1.128)),

$$\psi^{(1)}(\mathbf{q},\tau) = \nabla_{\mathbf{q}} \cdot \mathbf{\Psi}^{(1)}(\mathbf{q},\tau) = -D_1(\tau)\,\delta(\mathbf{q}), \tag{1.131}$$

and the divergence of the second order solution describes the tidal effects,

$$\psi^{(2)}(\mathbf{q},\tau) = \nabla_{\mathbf{q}} \cdot \mathbf{\Psi}^{(2)}(\mathbf{q},\tau) = \frac{1}{2}\frac{D_2(\tau)}{D_1^2(\tau)} \sum_{i\neq j} \left[\mathbf{\Psi}^{(1)}_{i,i}\mathbf{\Psi}^{(1)}_{j,j} - \mathbf{\Psi}^{(1)}_{i,j}\mathbf{\Psi}^{(1)}_{j,i} \right], \tag{1.132}$$

where $\mathbf{\Psi}^{(1)}_{k,l} \equiv \partial \mathbf{\Psi}^{(1)}_k / \partial \mathbf{q}_l$ and $D_2(\tau)$ denotes the second-order growth factor, defined in section 1.4.3.

Lagrangian potentials. Since Lagrangian solutions up to second order are irrotational (Melott, Buchert & Weiß, 1995; Buchert, Melott & Weiß, 1994; Bernardeau *et al.*, 2002; this is assuming that initial conditions are only in the growing mode, in the same spirit as neglecting completely the decaying vorticity), it is convenient to define the Lagrangian potentials $\phi^{(1)}$ and $\phi^{(2)}$ from which $\mathbf{\Psi}^{(1)}$ and $\mathbf{\Psi}^{(2)}$ derive, so that in 2LPT,

$$\mathbf{\Psi}^{(1)}(\mathbf{q},\tau) = -D_1(\tau)\nabla_{\mathbf{q}}\phi^{(1)}(\mathbf{q}) \quad \text{and} \quad \mathbf{\Psi}^{(2)}(\mathbf{q},\tau) = D_2(\tau)\nabla_{\mathbf{q}}\phi^{(2)}(\mathbf{q}). \tag{1.133}$$

Since $\mathbf{\Psi}^{(1)}$ is of order $D_1(\tau)$ (equation (1.131)) and $\mathbf{\Psi}^{(2)}(\tau)$ is of order $D_2(\tau)$ (equation (1.132)), the above potentials are time-independent. They satisfy Poisson-like equations (Buchert, Melott & Weiß, 1994),

$$\Delta_{\mathbf{q}}\phi^{(1)}(\mathbf{q}) = \delta(\mathbf{q}), \tag{1.134}$$

$$\Delta_{\mathbf{q}}\phi^{(2)}(\mathbf{q}) = \sum_{i>j} \left[\phi^{(1)}_{,ii}(\mathbf{q})\phi^{(1)}_{,jj}(\mathbf{q}) - (\phi^{(1)}_{,ij}(\mathbf{q}))^2 \right]. \tag{1.135}$$

The mapping from Eulerian to Lagrangian, equation (1.130), thus reads

$$\mathbf{x}(\tau) = \mathbf{q} - D_1(\tau)\nabla_{\mathbf{q}}\phi^{(1)}(\mathbf{q}) + D_2(\tau)\nabla_{\mathbf{q}}\phi^{(2)}(\mathbf{q}). \tag{1.136}$$

Velocity field in second-order Lagrangian perturbation theory. Taking the derivative of the previous equation yields for the velocity field,

$$\mathbf{u} = -f_1(\tau)D_1(\tau)\mathcal{H}(\tau)\nabla_{\mathbf{q}}\phi^{(1)}(\mathbf{q}) + f_2(\tau)D_2(\tau)\mathcal{H}(\tau)\nabla_{\mathbf{q}}\phi^{(2)}(\mathbf{q}). \tag{1.137}$$

which involves the logarithmic derivatives of the growth factors, $f_i \equiv \mathrm{d}\ln D_i/\mathrm{d}\ln a$, well approximated in a flat ΛCDM model by (Bouchet *et al.*, 1995)

$$f_1 \approx \Omega_\mathrm{m}^{5/9} \quad \text{and} \quad f_2 \approx 2\,\Omega_\mathrm{m}^{6/11} \approx 2\,f_1^{54/55}. \tag{1.138}$$

Other expressions for different cosmologies can be found in Bouchet *et al.* (1995); Bernardeau *et al.* (2002).

1.6 Non-linear approximations to gravitational instability

When fluctuations become strongly non-linear in the density field, Eulerian perturbation theory breaks down. Lagrangian perturbation theory is often more successful, since the Lagrangian picture is intrinsically non-linear in the density field (see e.g. equation (1.125)). A small perturbation in the Lagrangian displacement field carries a considerable amount of non-linear information about the corresponding Eulerian density and velocity fields. However, at some point, computers are required to study gravitational instability (in particular through N-body simulations), the important drawback being that the treatment becomes numerical instead of analytical. We will adopt this approach in this thesis. However, several non-linear approximations to the equations of motion have been suggested in the literature to allow the extrapolation of analytical calculations in the non-linear regime. We now briefly review some of them (see also Melott, 1994; Sahni & Coles, 1995).

Non-linear approximations consist of replacing one of the equations of the dynamics (Poisson – equation (1.72) –, continuity – equation (1.79) – or Euler – equation (1.80)) by a different assumption.[4] In general, the Poisson equation is replaced (Munshi & Starobinsky, 1994). These modified dynamics are often local, in the sense described above for the ZA, in order to provide a simpler way of calculating the evolution of fluctuations than the full non-local dynamics.

1.6.1 The Zel'dovich approximation as a non-linear approximation

As we have seen in section 1.3, in Eulerian dynamics, non-linearity is encoded in the Poisson equation, equation (1.72), $\Delta\Phi = 4\pi \mathrm{G} a^2 \bar{\rho}\delta$. The goal of this paragraph is to see what replaces the Poisson equation in the Eulerian description of the ZA. From this point of view, the ZA is the original non-linear Eulerian approximation, and it remains one of the most famous.

If we restrict our attention to potential movements, the peculiar velocity field $\mathbf{u}$ is irrotational. It can be written as the gradient of a velocity potential,

$$\mathbf{u} = -\frac{\nabla_{\mathbf{x}} V}{a}. \tag{1.139}$$

As discussed before, the main reason to restrict to this case is the decay of vortical perturbations.

It is then possible to postulate various forms for the velocity potential V. The ZA corresponds to the Ansatz (Munshi & Starobinsky, 1994; Hui & Bertschinger, 1996; appendix B in Scoccimarro, 1997)

$$V = \frac{2fa}{3\Omega_\mathrm{m}\mathcal{H}}\Phi, \tag{1.140}$$

where Φ is the cosmological gravitational potential and f is the logarithmic derivative of the linear growth factor. The Zel'dovich approximation is therefore equivalent to the replacement of the Poisson equation by

$$\mathbf{u} = -\frac{2f}{3\Omega_\mathrm{m}\mathcal{H}}\nabla\Phi. \tag{1.141}$$

This can be explicitly checked as follows. Combining equations (1.124) and (1.141), one gets

$$\frac{\partial \mathbf{u}}{\partial \tau} + \mathcal{H}\mathbf{u} = \frac{3\Omega_\mathrm{m}\mathcal{H}}{2f}\mathbf{u}. \tag{1.142}$$

Then, noting that $\nabla_{\mathbf{q}} \cdot \mathbf{u} = \psi'$, the differential equation for ψ is

$$\psi'' + \mathcal{H}\psi' = \frac{3\Omega_\mathrm{m}\mathcal{H}}{2f}\psi', \tag{1.143}$$

Using the time evolution of D_1 (equation (1.94)) and the identity $D_1' = \mathcal{H} f D_1$, one can check that the Zel'dovich solution, $\psi = -D_1\delta(\mathbf{q})$ indeed verifies the above equation.

Equation (1.141) means that at linear order, particles just go straight (in comoving coordinates) in the direction set by their initial velocity. In the Zel'dovich approximation, the proportionality between velocity field and gravitational field always holds (not just to first order in $\mathbf{\Psi}$).

[4] In this section, we have come back to a Eulerian description of the cosmological fluid.

Note that during the matter era, $a \propto t^{2/3}$ and thus $\mathcal{H} \equiv \dot{a} = 2a/(3t)$, which means that an equivalent form for the ZA Ansatz is

$$V = \frac{f}{\Omega_\mathrm{m}} \Phi t \approx \Phi t. \tag{1.144}$$

The ZA is a local approximation that represents exactly the true dynamics in one-dimensional collapse (Buchert, 1989; Yoshisato *et al.*, 2006). It is also possible to formulate local approximations that besides describing correctly planar collapse like the ZA, are suited for cylindrical or spherical collapse (leading to the formation of cosmic filaments and halos, in addition to cosmic pancakes). These approximations, namely the "non-magnetic" approximation (NMA, Bertschinger & Jain, 1994) and the "local tidal" approximation (LTA, Hui & Bertschinger, 1996), are not straightforward to implement for the calculation of statistical properties of density and velocity fields.

1.6.2 Other velocity potential approximations

Some other possibilities for the velocity potential can be found in literature (Coles, Melott & Shandarin, 1993; Munshi & Starobinsky, 1994). The frozen flow (FF) approximation (Matarrese *et al.*, 1992) postulates

$$V = \Phi^{(1)} t, \tag{1.145}$$

where $\Phi^{(1)}$ is the first-order solution (the linear approximation) for the gravitational potential. It satisfies the Poisson equation in the linear regime,

$$\Delta \Phi^{(1)} = \frac{3}{2} \Omega_\mathrm{m}(\tau) \mathcal{H}^2(\tau) \delta_1(\mathbf{x}, \tau), \tag{1.146}$$

where $\delta_1(\mathbf{x}, \tau) = D_1(\tau)\, \delta_1(\mathbf{x})$ is the linearly extrapolated density field. In FF, the Poisson equation is replaced by the analog of equation (1.141), substituting equation (1.145),

$$\mathbf{u} = -\frac{2f}{3\Omega_\mathrm{m}\mathcal{H}} \nabla \Phi^{(1)}, \tag{1.147}$$

or, by taking the divergence and using equation (1.146),

$$\theta(\mathbf{x}, \tau) = -\mathcal{H}(\tau) f\, \delta_1(\mathbf{x}, \tau). \tag{1.148}$$

The physical meaning of this approximation is that the velocity field is assumed to remain linear while the density field is allowed to explore the non-linear regime.

In the linearly-evolving potential (LEP) approximation (Brainerd, Scherrer & Villumsen, 1993; Bagla & Padmanabhan, 1994), the gravitational potential is instead assumed to remain the same as in the linear regime; therefore, the Poisson equation is replaced by

$$\Phi = \Phi^{(1)}, \quad \Delta \Phi = \frac{3}{2} \Omega_\mathrm{m}(\tau) \mathcal{H}^2(\tau) \delta_1(\mathbf{x}, \tau). \tag{1.149}$$

The idea is that since $\Phi \propto \delta/k^2$ in Fourier space, the gravitational potential is dominated by the long-wavelength modes more than the density field, and therefore it ought to obey linear perturbation theory to a better approximation.

1.6.3 The adhesion approximation

All the above approximations (ZA, NMA, LTA, FF, LP) are local, which means that we neglect the self-gravity of inhomogeneities. A significant problem of the ZA, and of subsequent variations, is the fact that after shell-crossing, matter continues to flow throughout the newly-formed structure, which should instead be gravitationally bound. This phenomenon washes out cosmic structures on small scales.

A possible phenomenological solution is to add a viscosity term to the single-stream Euler equation, equation (1.85), which then becomes Burgers' equation,

$$\frac{\partial \mathbf{u}_i(\mathbf{x}, \tau)}{\partial \tau} + \mathcal{H}(\tau) \mathbf{u}_i(\mathbf{x}, \tau) + \mathbf{u}_j(\mathbf{x}, \tau) \cdot \nabla_j \mathbf{u}_i(\mathbf{x}, \tau) = -\nabla_i \Phi(\mathbf{x}, \tau) + v\, \Delta \mathbf{u}_i(\mathbf{x}, \tau). \tag{1.150}$$

This is the so-called *adhesion approximation* (Kofman & Shandarin, 1988; Gurbatov, Saichev & Shandarin, 1989; Kofman *et al.*, 1992; Valageas & Bernardeau, 2011; Hidding *et al.*, 2012). For a potential flow, it can be reduced to a linear diffusion equation, and therefore solved exactly. Surprisingly, in the adhesion approximation, the dynamical equations describing the evolution of the self-gravitating cosmological fluid can be written in the form of a Schrödinger equation coupled to a Poisson equation describing Newtonian gravity (Short & Coles, 2006b). The dynamics can therefore be studied with the tools of wave mechanics. An alternative to the adhesion model is the free-particle approximation (FPA), in which the artificial viscosity term in Burgers' equation is replaced by a non-linear term known as the *quantum pressure*. This also leads to a free-particle Schrödinger equation (Short & Coles, 2006b,a).

Comparisons of the adhesion approximation to full-gravitational numerical simulations show an improvement over the ZA at small scales, even if the fragmentation of structures into dense clumps is still underestimated (Weinberg & Gunn, 1990). At weakly non-linear scales, the adhesion approximation is essentially equal to the ZA.

Chapter 2

Numerical diagnostics of Lagrangian perturbation theory

Contents

2.1 Correlation functions of the density field **30**
2.1.1 One-point statistics 30
2.1.2 Two-point statistics 31
2.1.3 Three-point statistics 34
2.2 Statistics of the Lagrangian displacement field **37**
2.2.1 Lagrangian ψ versus Eulerian δ: one-point statistics 37
2.2.2 Perturbative and non-perturbative prescriptions for ψ 41
2.2.3 Non-linear evolution of ψ and generation of a vector part 43
2.3 Comparison of structure types in LPT and N-body dynamics **44**

"**Hector Barbossa**: The world used to be a bigger place.
Jack Sparrow: The world's still the same. There's just... less in it."
— Pirates of the Caribbean: At World's End (2007)

Abstract

This chapter is intended as a guide on the approximation error in using Lagrangian perturbation theory instead of fully non-linear gravity in large-scale structure analysis. We compare various properties of particle realizations produced by LPT and by N-body simulations. In doing so, we characterize differences and similarities, as a function of scale, resolution and redshift.

The goal of this chapter is to characterize the accuracy of Lagrangian perturbation theory in terms of a set of numerical diagnostics. It is organized as follows. In section 2.1, we look at the correlations functions of the density field, which usually are the final observable in cosmological surveys. As the displacement field plays a central role in LPT, we study its statistics in section 2.2. In particular, we illustrate that in some regimes, when the perturbative parameter is large, 2LPT performs worse than the ZA. We examine the decomposition of the displacement field in a scalar and rotational part and review various approximations based on its divergence. Finally, in section 2.3, we compare cosmic web elements (voids, sheets, filaments, and clusters) as predicted by LPT and by non-linear simulations of the LSS.[1]

Corresponding LPT and N-body simulations used in this chapter have been run from the same initial conditions, generated at redshift $z = 63$ using second-order Lagrangian perturbation theory. The N-body simulations have been run with the Gadget-2 cosmological code (Springel, Yoshida & White, 2001; Springel, 2005). Evolutions of the Zel'dovich approximation were performed with N-GenIC (Springel, 2005), and of second-order Lagrangian perturbation theory with 2LPTic (Crocce, Pueblas & Scoccimarro, 2006a). To ensure sufficient statistical significance, we used eight realizations of the same cosmology, changing the seed used to generate respective initial conditions. All computations are done after binning the dark matter particles with a Cloud-in-Cell (CiC) method (see section B.3). The simulations contain 512^3 particles in a 1024 Mpc/h cubic box with periodic boundary conditions. We checked that with this setup, the power spectrum agrees with

[1] In the following, we will often write "full gravity", even if, strictly speaking, N-body simulations also involve some degree of approximation.

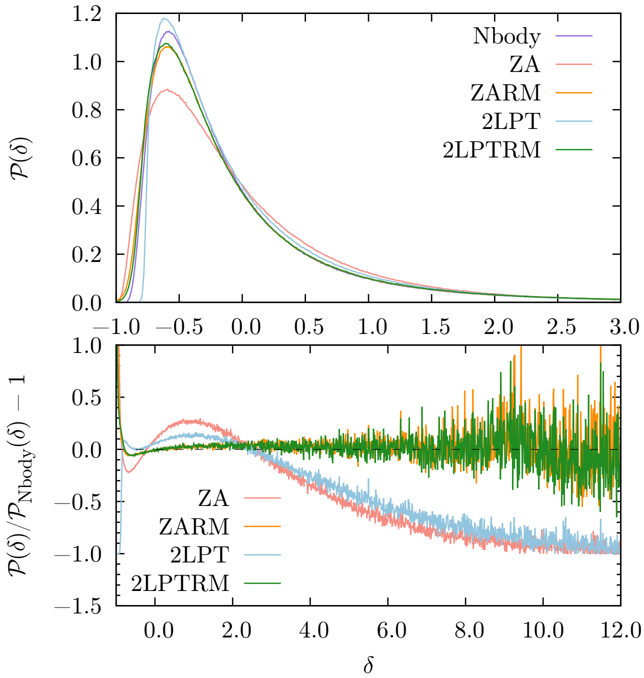

Figure 2.1: *Upper panel.* Redshift-zero probability distribution function for the density contrast δ, computed from eight 1024 Mpc/h-box simulations of 512^3 particles. The particle distribution is determined using: a full N-body simulation (purple curve), the Zel'dovich approximation, alone (ZA, light red curve) and after remapping (ZARM, orange curve), second-order Lagrangian perturbation theory, alone (2LPT, light blue curve) and after remapping (2LPTRM, green curve). *Lower panel.* Relative deviations of the same pdfs with reference to N-body simulation results. Note that, contrary to standard LPT approaches, remapped fields follow the one-point distribution of full N-body dynamics in an unbiased way, especially in the high density regime.

the non-linear power spectrum of simulations run with higher mass resolution, provided by COSMIC EMULATOR tools (Heitmann *et al.*, 2009, 2010; Lawrence *et al.*, 2010) (deviations are at most sub-percent level for $k \lesssim 1$ (Mpc/h)$^{-1}$). Therefore, at the scales of interest of this work, $k \leq 0.4$ (Mpc/h)$^{-1}$ (corresponding to the linear and mildly non-linear regime at redshift zero), the clustering of dark matter is correctly reproduced by our set of simulations.

The cosmological parameters used are WMAP-7 fiducial values (Komatsu *et al.*, 2011),

$$\Omega_\Lambda = 0.728, \Omega_{\rm m} = 0.2715, \Omega_{\rm b} = 0.0455, \sigma_8 = 0.810, h = 0.704, n_{\rm s} = 0.967. \tag{2.1}$$

Thus, each particle carries a mass of 6.03×10^{11} M$_\odot/h$.

2.1 Correlation functions of the density field

This section draws from section III in Leclercq *et al.* (2013).

In this section, we analyze the correlation functions of the density contrast field, δ, in LPT and N-body fields.

Note. All plots presented in this section contain lines labeled as "ZARM" and "2LPTRM" which correspond to remapped fields based on the ZA and on 2LPT, respectively. They are ignored in this chapter, which focuses on diagnostics of LPT. For a description of the remapping procedure and for comments on these approximations in comparison to the ZA, 2LPT and N-body dynamics, the reader is referred to chapter 6.

2.1.1 One-point statistics

Figure 2.1 shows the pdf for the density contrast, $\mathcal{P}_\delta$, at redshift zero, for N-body simulations, and for ZA and 2LPT density fields. All pdfs are non-Gaussian with a substantial skewness, are tied down to 0 at $\delta = -1$

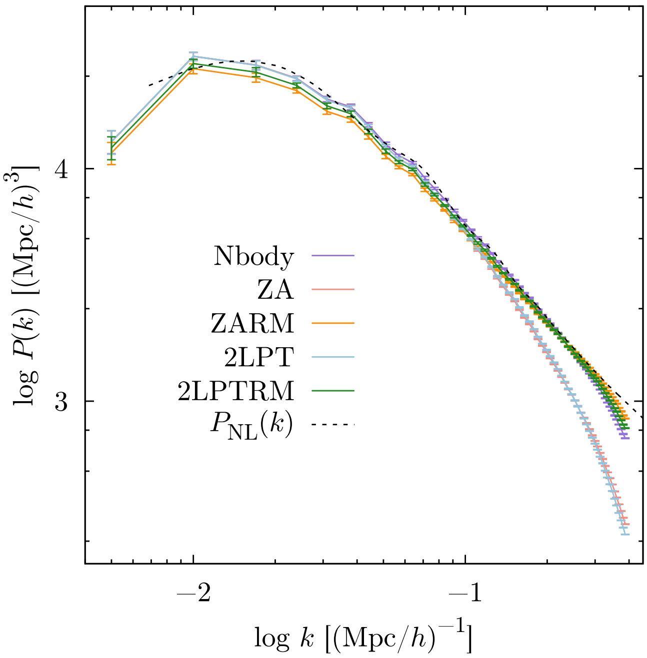

Figure 2.2: Redshift-zero dark matter power spectra in a 1024 Mpc/h simulation, with density fields computed with a mesh size of 8 Mpc/h. The particle distribution is determined using: a full N-body simulation (purple curve), the Zel'dovich approximation, alone (ZA, light red curve) and after remapping (ZARM, orange curve), second-order Lagrangian perturbation theory, alone (2LPT, light blue curve) and after remapping (2LPTRM, green curve). The dashed black curve represents $P_{\mathrm{NL}}(k)$, the theoretical power spectrum expected at $z = 0$. Both ZARM and 2LPTRM show increased power in the mildly non-linear regime compared to ZA and 2LPT (at scales corresponding to $k \gtrsim 0.1$ (Mpc/h)$^{-1}$ for this redshift), indicating an improvement of two-point statistics with the remapping procedure.

with a large tail in the high-density values. As discussed in section 1.2.3.4, the late-time pdf for density fields is approximately log-normal. However, already at the level of one-point statistics, the detailed behaviors of LPT and N-body simulations disagree: the peak of the pdf is shifted and the tails differ. In particular, LPT largely underpredicts the number of voxels in the high-density regime. This effect is more severe for the ZA than for 2LPT. This comes from the fact that 2LPT captures some of non-local effects involved in the formation of the densest halos.

The one-point pdf of the density is further analyzed in section 2.2.1, in comparison to the one-point pdf of the Lagrangian displacement field.

2.1.2 Two-point statistics

2.1.2.1 Power spectrum

We measured the power spectrum of dark matter density fields, as defined by equation (1.41). Dark matter particles have been displaced according to each prescription and assigned to cells with a CiC scheme, for different mesh sizes. Power spectra were measured from theses meshes, with a correction for aliasing effects (Jing, 2005). Redshift-zero results computed on a 8 Mpc/h mesh are presented in figure 2.2. There, the dashed line corresponds to the theoretical, non-linear power spectrum expected, computed with Cosmic Emulator tools (Heitmann *et al.*, 2009, 2010; Lawrence *et al.*, 2010). A deviation of full N-body simulations from this theoretical prediction can be observed at small scales. This discrepancy is a gridding artifact, completely due to the finite mesh size used for the analysis. As a rule of thumb, a maximum threshold in k for trusting the simulation data is set by a quarter of the Nyquist wavenumber, defined by $k_{\mathrm{N}} \equiv 2\pi/L \times N_{\mathrm{p}}^{1/3}/2$, where L is the size of the box and N_{p} is the number of cells in the Lagrangian grid on which particles are placed in the initial conditions; which makes for our analysis ($L = 1024$ Mpc/h, $N_{\mathrm{p}} = 512^3$), $k_{\mathrm{N}}/4 \approx 0.39$ (Mpc/h)$^{-1}$. At this scale, it has been observed that the power spectrum starts to deviate at the percent-level with respect to higher resolution simulations (Heitmann *et al.*, 2010). The relative deviations of various power spectra with reference

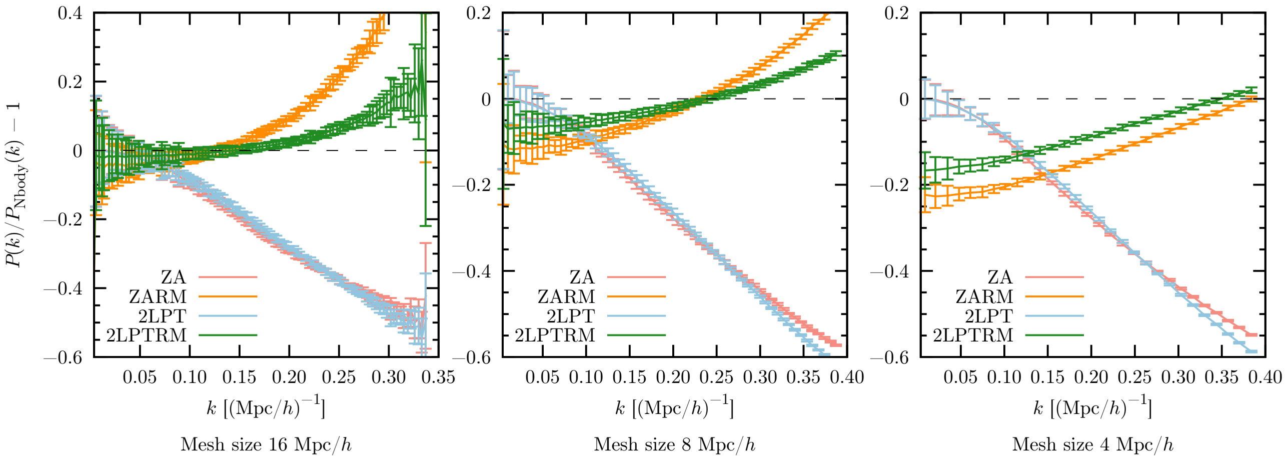

Figure 2.3: *Power spectrum: mesh size-dependence.* Relative deviations for the power spectra of various particle distributions, with reference to the density field computed with a full N-body simulation. The particle distribution is determined using: the Zel'dovich approximation, alone (ZA, light red curve) and after remapping (ZARM, orange curve), second-order Lagrangian perturbation theory, alone (2LPT, light blue curve) and after remapping (2LPTRM, green curve). The computation is done on different meshes: 16 Mpc/h (64^3-voxel grid, left panel), 8 Mpc/h (128^3-voxel grid, central panel) and 4 Mpc/h (256^3-voxel grid, right panel). All results are shown at redshift $z = 0$. LPT fields exhibit more small-scale correlations after remapping and their power spectra get closer to the shape of the full non-linear power spectrum.

to full gravity are presented in figures 2.3 and 2.4. In all the plots, the error bars represent the dispersion of the mean among eight independent realizations.

Generally, LPT correctly predicts the largest scales, when $k \to 0$ (the smallest wavelength mode accessible here is set by the box size: $k_{\mathrm{min}} = 2\pi/L$ with $L = 1024$ Mpc/h, giving $k_{\mathrm{min}} \approx 0.006$ (Mpc/h)$^{-1}$), as these are in the linear regime. These are affected by cosmic variance, but the effect is not visible in our plots, as corresponding LPT and N-body fields start from the same initial conditions. Differences arise in the mildly non-linear and non-linear regime, where LPT predicts too little power. Indeed, as LPT only captures part of the non-linearity of the Vlasov-Poisson system, presented in section 1.3.1, the clustering of dark matter particles is underestimated.

The discrepancy between LPT and N-body power spectra depends both on the target resolution (see figure 2.3) and on the desired redshift (see figure 2.4). For example, at a resolution of 8 Mpc/h and at a comoving wavelength of $k = 0.40$ (Mpc/h)$^{-1}$, 2LPT only lacks 5% power at $z = 3$ but more than 50% at $z = 0$. At fixed redshift, the lack of small scale power in LPT weakly depends on the mesh size.

2.1.2.2 Fourier-space cross-correlation coefficient

The Fourier space cross-correlation coefficient between two density fields δ and δ' is defined as the cross-power spectrum of δ and δ', normalized by the auto-power spectra of the same fields:

$$R(k) \equiv \frac{P_{\delta\times\delta'}(k)}{\sqrt{P_\delta(k)P_{\delta'}(k)}} \equiv \frac{\langle\delta^*(\mathbf{k})\delta'(\mathbf{k})\rangle}{\sqrt{\langle\delta^*(\mathbf{k})\delta(\mathbf{k})\rangle\,\langle\delta'^*(\mathbf{k})\delta'(\mathbf{k})\rangle}}. \tag{2.2}$$

It is a dimensionless coefficient, in modulus between 0 and 1, representing the agreement, at the level of two-point statistics, between the *phases* of δ and δ' (as the overall power has been divided out). Here we choose as a reference the density field predicted by N-body simulations, $\delta' = \delta_{\mathrm{Nbody}}$, and compare with approximate density fields generated from the same initial conditions with LPT. In this fashion, we characterize the phase accuracy of the ZA and 2LPT.

In figure 2.5 we present the Fourier-space cross-correlation coefficient between the redshift-zero density field in the N-body simulation and other density fields. At this point, it is useful to recall that an approximation well-correlated with the non-linear density field can be used in a variety of cosmological applications, such as the reconstruction of the non-linear power spectrum (Tassev & Zaldarriaga, 2012c). As pointed out by Neyrinck (2013), the cross-correlation between 2LPT and full gravitational dynamics is higher at small k than the cross-

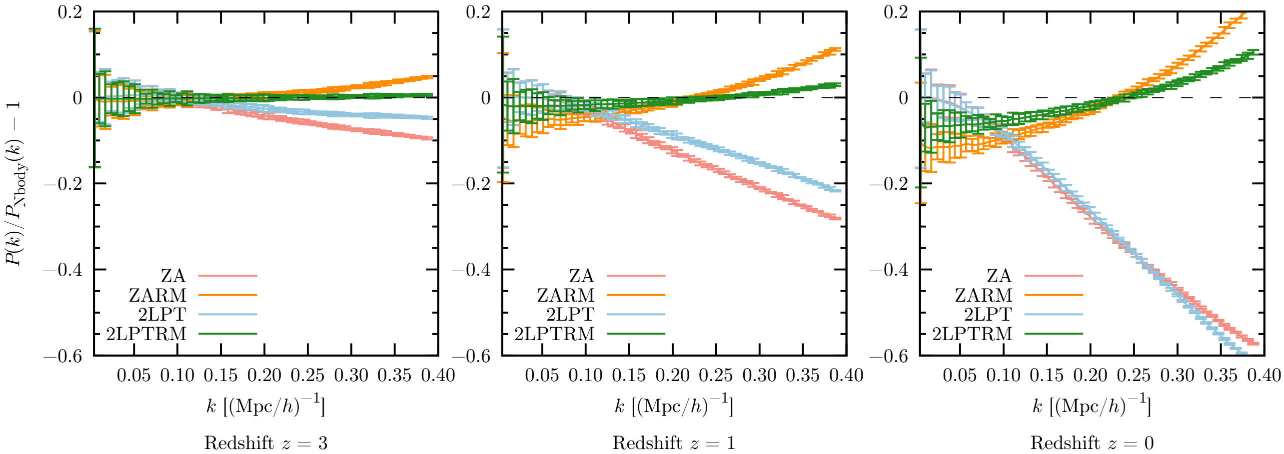

Figure 2.4: *Power spectrum: redshift-dependence.* Relative deviations for the power spectra of various particle distributions (see the caption of figure 2.3), with reference to the density field computed with a full N-body simulation. The computation is done on a 8 Mpc/h mesh (128^3-voxel grid). Results at different redshifts are shown: $z = 3$ (right panel), $z = 1$ (central panel) and $z = 0$ (left panel). The remapping procedure is increasingly successful with increasing redshift.

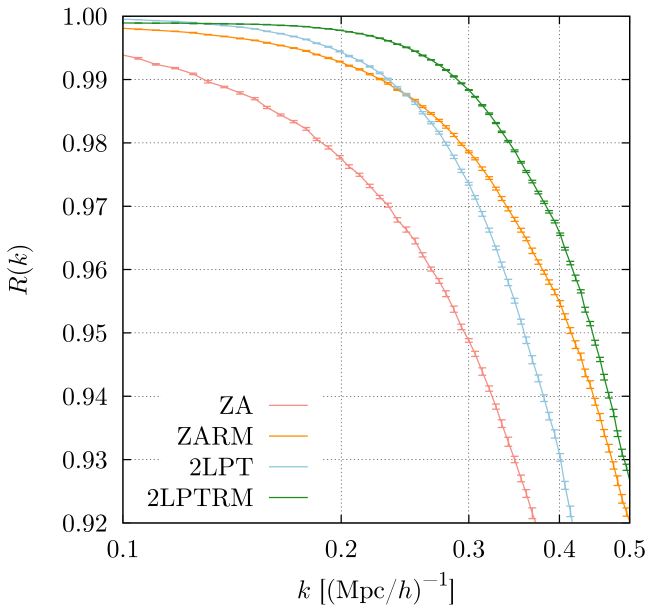

Figure 2.5: Fourier-space cross-correlation coefficient between various approximately-evolved density fields and the particle distribution as evolved with full N-body dynamics, all at redshift zero. The binning of density fields is done on a 8 Mpc/h mesh (128^3-voxel grid). At small scales, $k \geq 0.2$ (Mpc/h)$^{-1}$, the cross-correlations with respect to the N-body-evolved field are notably better after remapping than with LPT alone.

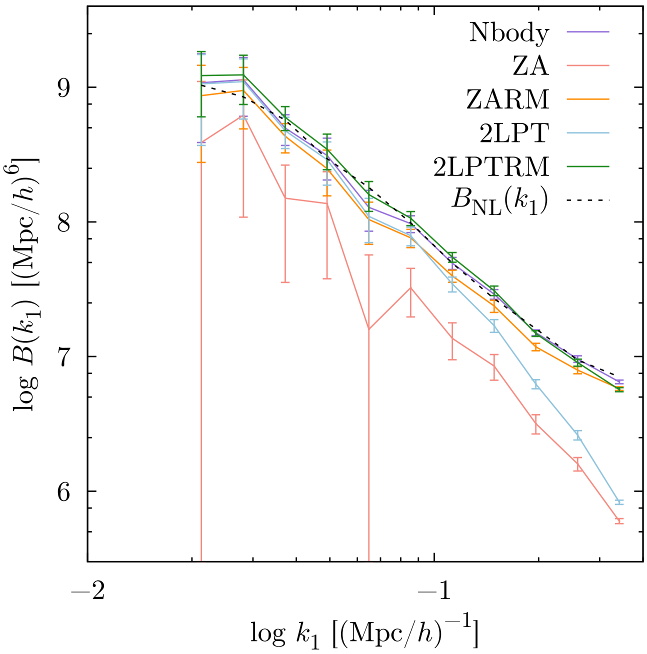

Figure 2.6: Redshift-zero dark matter bispectra for equilateral triangle shape, in 1024 Mpc/h simulations, with density fields computed on mesh of 8 Mpc/h size. The particle distribution is determined using: a full N-body simulation (purple curve), the Zel'dovich approximation, alone (ZA, light red curve) and after remapping (ZARM, orange curve), second-order Lagrangian perturbation theory, alone (2LPT, light blue curve) and after remapping (2LPTRM, green curve). The dashed line, $B_{\rm NL}(k)$, corresponds to theoretical predictions for the bispectrum, found using the fitting formula of (Gil-Marín *et al.*, 2012). Note that both ZARM and 2LPTRM show increased bispectrum in the mildly non-linear regime compared to ZA and 2LPT, indicating an improvement of three-point statistics with the remapping procedure.

correlation between the ZA and the full dynamics, meaning that the position of structures is more correct when additional physics (non-local tidal effects) is taken into account.

2.1.3 Three-point statistics

In this section, we analyze the accuracy of LPT beyond second-order statistics, by studying the three-point correlation function of the density field in Fourier space, i.e. the bispectrum, defined by equation (1.56). The importance of three-point statistics relies in their ability to test the shape of structures. Some of the natural applications are to test gravity (Shirata *et al.*, 2007; Gil-Marín *et al.*, 2011), to break degeneracies due to the galaxy bias (Matarrese, Verde & Heavens, 1997; Verde *et al.*, 1998; Scoccimarro *et al.*, 2001; Verde *et al.*, 2002) or to test the existence of primordial non-Gaussianities in the initial matter density field (Sefusatti & Komatsu, 2007; Jeong & Komatsu, 2009).

As for the power spectrum, we construct the dark matter density contrast field, by assigning particles to the grid using a CiC scheme. We then deconvolve the CiC kernel to correct for corresponding smoothing effects. The algorithm used to compute the bispectrum $B(\mathbf{k}_1, \mathbf{k}_2, \mathbf{k}_3)$ from this $\delta(\mathbf{k})$ field consists of randomly drawing k-vectors from a specified bin, namely Δk, and randomly orientating the $(\mathbf{k}_1, \mathbf{k}_2, \mathbf{k}_3)$ triangle in space. We chose the number of random triangles to depend on the number of fundamental triangle per bin, that scales as $k_1 k_2 k_3 \Delta k^3$ (Scoccimarro, 1997), where Δk is the chosen k-binning: given k_i we allow triangles whose i-side lies between $k_i - \Delta k/2$ and $k_i + \Delta k/2$. In this paper we always set $\Delta k = k_{\rm min} = 2\pi/L$, where L is the size of the box. For the equilateral case, at scales of $k \approx 0.1$ (Mpc/h)$^{-1}$ we generate $\sim 1.7 \times 10^6$ random triangles. We have verified that increasing the number of triangles beyond this value does not have any effect on the measurement. The rule of thumb presented in section 2.1.2.1 for the smallest scale to trust applies for the bispectrum as well. Also, as a lower limit in k, we have observed that for scales larger than $\sim 3\,k_{\rm min}$, effects of cosmic variance start to be important and considerable deviations with respect to linear theory can be observed. For this reason, we limit the largest scale for our bispectrum analysis to $3\,k_{\rm min} \approx 1.8 \times 10^{-2}$ (Mpc/h)$^{-1}$.

Error bars in bispectrum plots represent the dispersion of the mean among eight independent realizations, all

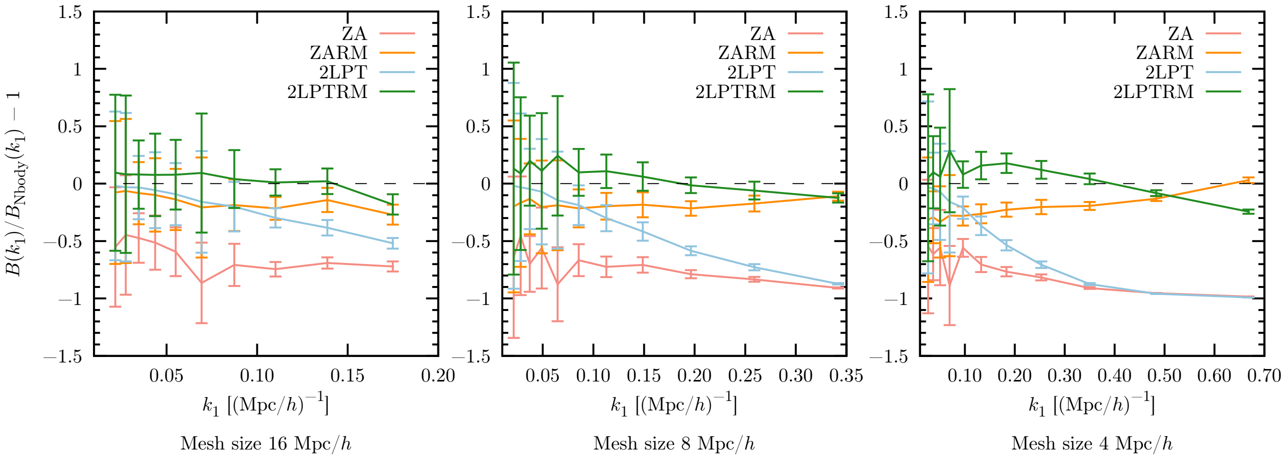

Figure 2.7: *Bispectrum: mesh size-dependence.* Relative deviations for the bispectra $B(k_1)$ of various particle distributions, with reference to the prediction from a full N-body simulation, $B_{\mathrm{Nbody}}(k_1)$. The particle distribution is determined using: the Zel'dovich approximation, alone (ZA, light red curve) and after remapping (ZARM, orange curve), second-order Lagrangian perturbation theory, alone (2LPT, light blue curve) and after remapping (2LPTRM, green curve). The computation of bispectra is done for equilateral triangles and on different meshes: 16 Mpc/h (64^3-voxel grid, left panel), 8 Mpc/h (128^3-voxel grid, central panel) and 4 Mpc/h (256^3-voxel grid, right panel). All results are shown at redshift $z = 0$. LPT fields exhibit more small-scale three-point correlations after remapping and their bispectra get closer to the shape of the full non-linear bispectrum.

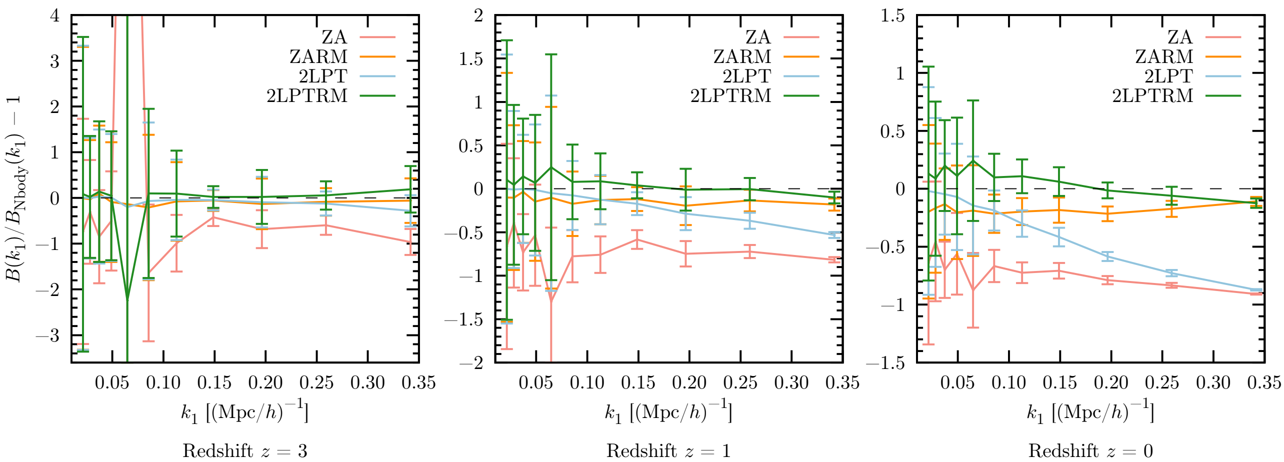

Figure 2.8: *Bispectrum: redshift-dependence.* Relative deviations for the bispectra $B(k_1)$ of various particle distributions (see the caption of figure 2.7), with reference to a full N-body simulation, $B_{\mathrm{Nbody}}(k_1)$. The computation of bispectra is done on a 8 Mpc/h mesh (128^3-voxel grid) and for equilateral triangles. Results at different redshifts are shown: $z = 3$ (right panel), $z = 1$ (central panel) and $z = 0$ (left panel).

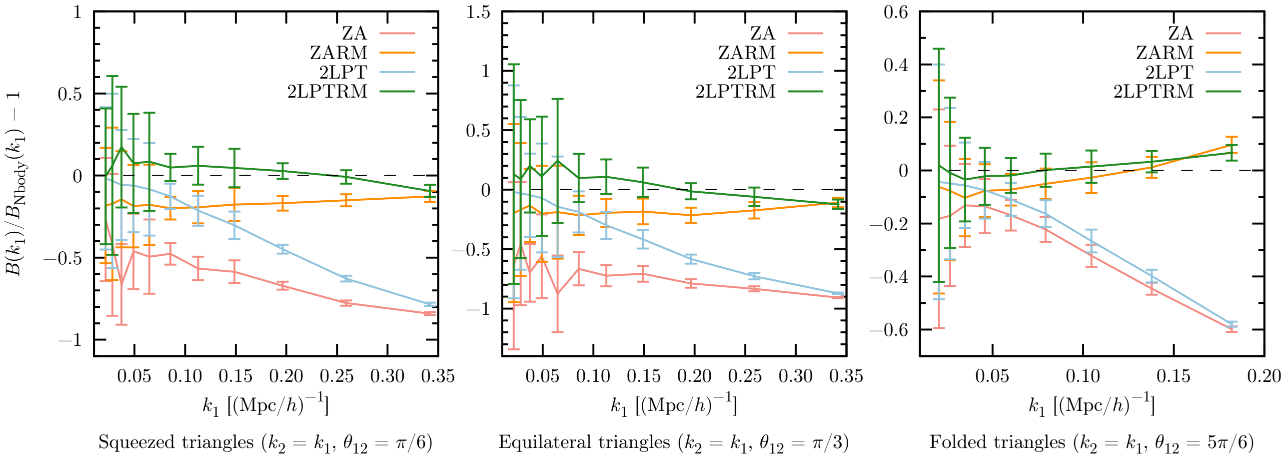

Figure 2.9: *Bispectrum: scale-dependence for different triangle shapes.* Relative deviations for the bispectra $B(k_1)$ of various particle distributions (see the caption of figure 2.7), with reference to a full N-body simulation, $B_{\mathrm{Nbody}}(k_1)$. The computation is done on a 8 Mpc/h mesh (128^3-voxel grid) and results are shown at redshift $z = 0$ for various triangle shapes as defined above.

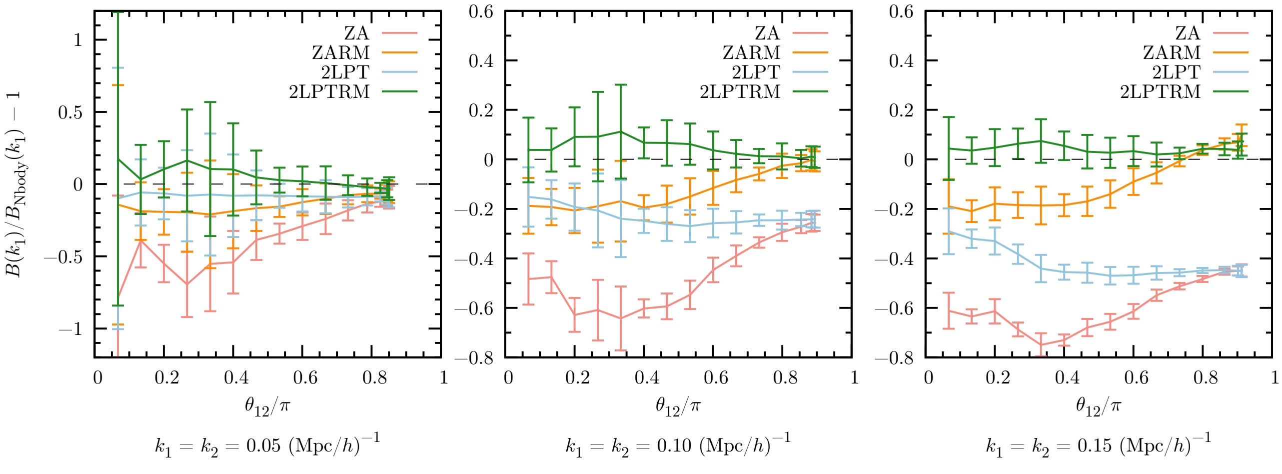

Figure 2.10: *Bispectrum: triangle shape-dependence.* Relative deviations for the bispectra $B(k_1)$ of various particle distributions (see the caption of figure 2.7), with reference to a full N-body simulation, $B_{\mathrm{Nbody}}(k_1)$. The computation is done on a 8 Mpc/h mesh (128^3-voxel grid) and results are shown at redshift $z = 0$. The dependence on the angle of the triangle $\theta_{12} = (\mathbf{k}_1, \mathbf{k}_2)$ is shown for different scales: $k_1 = k_2 = 0.05$ (Mpc/h)$^{-1}$ (corresponding to 125 Mpc/h), $k_1 = k_2 = 0.10$ (Mpc/h)$^{-1}$ (corresponding to 63 Mpc/h), $k_1 = k_2 = 0.15$ (Mpc/h)$^{-1}$ (corresponding to 42 Mpc/h).

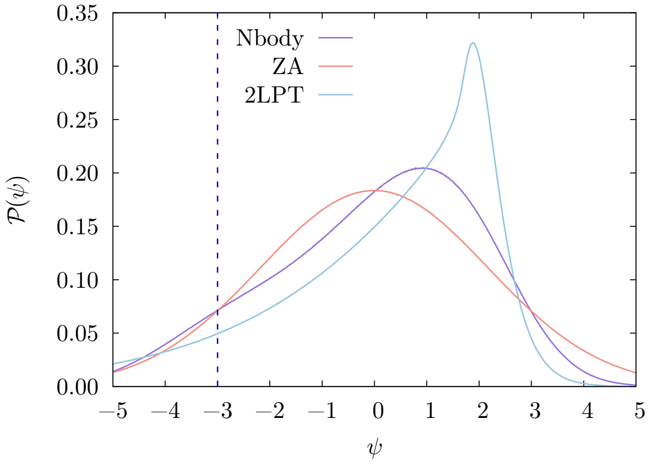

Figure 2.11: Redshift-zero probability distribution function for the divergence of the displacement field ψ, computed from eight 1024 Mpc/h-box simulations of 512^3 particles. A quantitative analysis of the deviation from Gaussianity of these pdfs is given in table 2.1. The particle distribution is determined using: a full N-body simulation (purple curve), the Zel'dovich approximation (ZA, light red curve) and second-order Lagrangian perturbation theory (2LPT, light blue curve). The vertical line at $\psi = -3$ represents the collapse barrier about which ψ values bob around after gravitational collapse. A bump at this value is visible with full gravity, but LPT is unable to reproduce this feature. This regime corresponds to virialized, overdense clusters.

of them with the same cosmological parameters. It has been tested (Gil-Marín *et al.*, 2012), that this estimator for the error is in good agreement with theoretical predictions based on the Gaussianity of initial conditions (Scoccimarro, 1998).

The subtracted shot noise is always assumed to be Poissonian:

$$B_{\mathrm{SN}}(\mathbf{k}_1, \mathbf{k}_2, \mathbf{k}_3) = \frac{1}{\bar{n}} \left[P(k_1) + P(k_2) + P(k_3)\right] + \frac{1}{\bar{n}^2}, \tag{2.3}$$

(see e.g. Peebles, 1980, and references therein), where $\bar{n}$ is the number density of particles in the box.

A triangle shape is defined by the relative length of vectors $\mathbf{k}_1$ and $\mathbf{k}_2$ and the inner angle θ_{12}, in such a way that $\mathbf{k}_1 + \mathbf{k}_2 + \mathbf{k}_3 = 0$ and $\mathbf{k}_1 \cdot \mathbf{k}_2 = k_1 k_2 \cos(\pi - \theta_{12})$. In figure 2.6, we plot the redshift-zero bispectrum, computed on a 8 Mpc/h mesh, of the different density fields for equilateral triangles ($\theta_{12} = \pi/3$ and $k_2/k_1 = 1$). There, the dashed line corresponds to theoretical predictions for the non-linear bispectrum, found using the fitting formula of Gil-Marín *et al.* (2012). The relative deviations of various bispectra with reference to full N-body simulations are shown in figures 2.7, 2.8, 2.9 and 2.10.

The main result is that LPT predicts less three-point correlation than full gravity. This is true even at large scales for the ZA: as it is local, it generally fails to predict the shape of structures. 2LPT agrees with N-body simulations at large scales, with differences starting to appear only in the mildly non-linear regime, $k \gtrsim 0.1$ (Mpc/h)$^{-1}$ at $z = 0$.

2.2 Statistics of the Lagrangian displacement field

2.2.1 Lagrangian ψ versus Eulerian δ: one-point statistics

This section draws from Leclercq, Jasche & Wandelt (2015b), addendum to Leclercq *et al.* (2013).

As noted by previous authors (see in particular Neyrinck, 2013), in the Lagrangian representation of the LSS, it is natural to use the divergence of the displacement field ψ instead of the Eulerian density contrast δ. This section comments the one-point statistics of ψ in LPT and full gravity and comparatively analyzes key features of ψ and δ.

As seen in section 1.5, in the Lagrangian frame, the quantity of interest is not the position, but the displacement field $\mathbf{\Psi}(\mathbf{q})$ which maps the initial comoving particle position $\mathbf{q}$ to its final comoving Eulerian position $\mathbf{x}$

Model	$\mathcal{P}_\delta$	$\mathcal{P}_\psi$
	Skewness γ_1	
ZA	2.36 ± 0.01	-0.0067 ± 0.0001
2LPT	2.83 ± 0.01	-1.5750 ± 0.0002
N-body	5.14 ± 0.05	-0.4274 ± 0.0001
	Excess kurtosis γ_2	
ZA	9.95 ± 0.09	$-2.2154 \times 10^{-6} \pm 0.0003$
2LPT	13.91 ± 0.15	3.544 ± 0.0011
N-body	62.60 ± 2.75	-0.2778 ± 0.0004

Table 2.1: Non-Gaussianity parameters (the skewness γ_1 and the excess kurtosis γ_2) of the redshift-zero probability distribution functions $\mathcal{P}_\delta$ and $\mathcal{P}_\psi$ of the density contrast δ and the divergence of the displacement field ψ, respectively. The confidence intervals given correspond to the 1-σ standard deviations among eight realizations. In all cases, γ_1 and γ_2 are reduced when measured from ψ instead of δ.

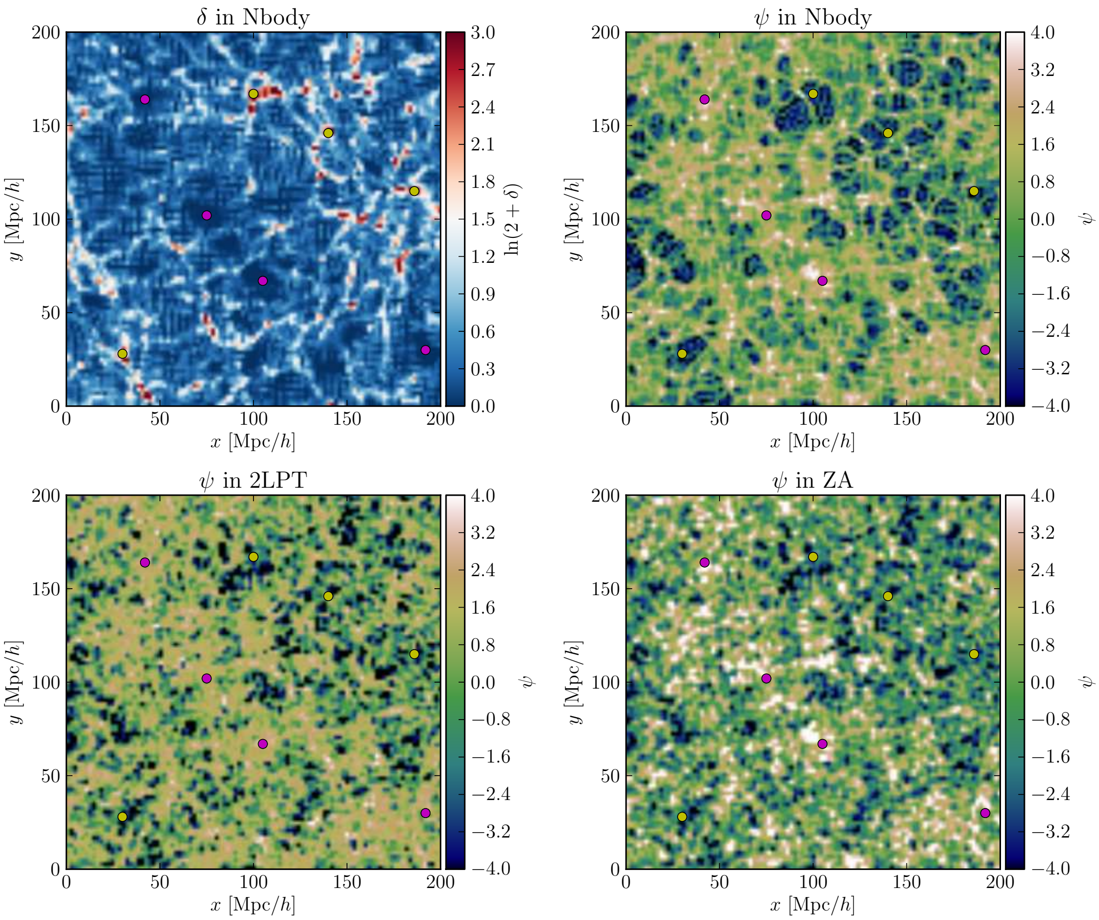

Figure 2.12: Slices of the divergence of the displacement field, ψ, on a Lagrangian sheet of 512^2 particles from a 512^3-particle simulation of box size 1024 Mpc/h, run to redshift zero. For clarity we show only a 200 Mpc/h region. Each pixel corresponds to a particle. The particle distribution is determined using respectively a full N-body simulation, the Zel'dovich approximation (ZA) and second-order Lagrangian perturbation theory (2LPT). In the upper left panel, the density contrast δ in the N-body simulation is shown, after binning on a 512^3-voxel grid. To guide the eye, some clusters and voids are identified by yellow and purple dots, respectively. The "lakes", Lagrangian regions that have collapsed to form halos, are only visible in the N-body simulation, while the "mountains", Lagrangian regions corresponding to cosmic voids, are well reproduced by LPT.

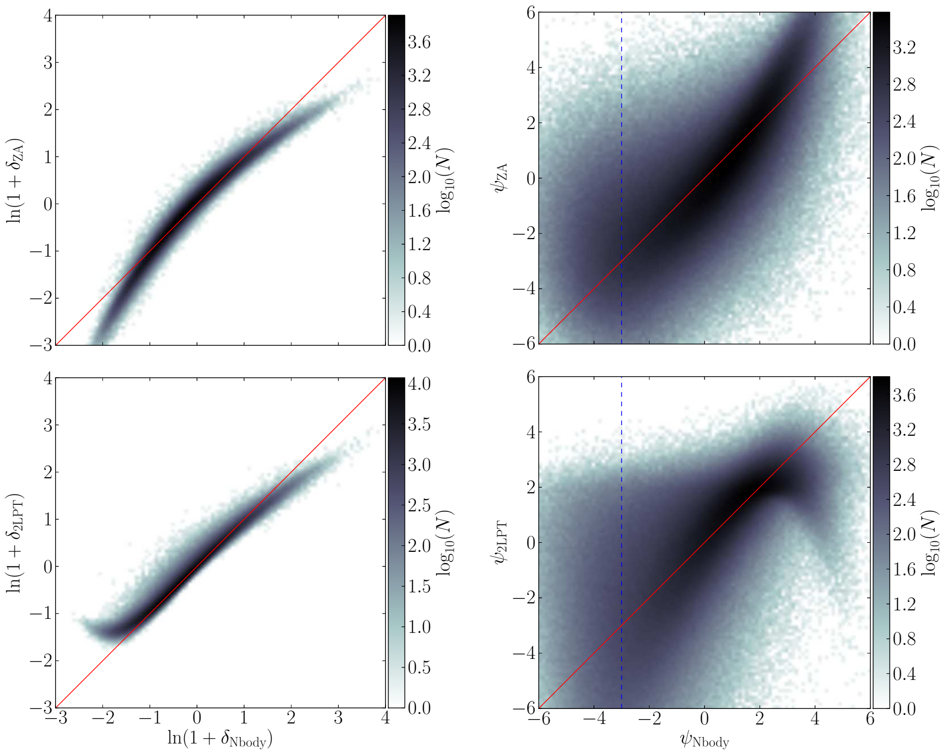

Figure 2.13: *Left panel.* Two-dimensional histograms comparing particle densities evolved with full N-body dynamics (the x-axis) to densities in the LPT-evolved particle distributions (the y-axis). The red lines show the ideal $y = x$ locus. A turn-up at low densities is visible with 2LPT, meaning that some overdense regions are predicted where there should be deep voids. *Right panel.* Same plot for the divergence of the displacement field ψ. Negative ψ corresponds to overdensities and positive ψ correspond to underdensities. The dotted blue line shows the collapse barrier at $\psi = -3$ where particle get clustered in full gravity. The scatter is bigger with ψ than with δ, in particular in overdensities, since with LPT, particles do not cluster. The turn-up at low densities with 2LPT, observed with the density contrast, is also visible with the divergence of the displacement field.

(see e.g. Bouchet *et al.*, 1995 or Bernardeau *et al.*, 2002 for overviews),

$$\mathbf{x} \equiv \mathbf{q} + \mathbf{\Psi}(\mathbf{q}). \tag{2.4}$$

It is important to note that, though $\mathbf{\Psi}(\mathbf{q})$ is *a priori* a full three-dimensional vector field, it is curl-free up to second order in LPT (appendix D in Bernardeau, 1994 or Bernardeau *et al.*, 2002 for a review). In this thesis, we do not consider perturbative contributions beyond 2LPT.

Let $\psi(\mathbf{q}) \equiv \nabla_{\mathbf{q}} \cdot \mathbf{\Psi}(\mathbf{q})$ denote the divergence of the displacement field, where $\nabla_{\mathbf{q}}$ is the divergence operator in Lagrangian coordinates. ψ quantifies the angle-averaged spatial-stretching of the Lagrangian dark matter "sheet" in comoving coordinates (Neyrinck, 2013). Let $\mathcal{P}_{\psi,\mathrm{LPT}}$ and $\mathcal{P}_{\psi,\mathrm{Nbody}}$ be the one-point probability distribution functions for the divergence of the displacement field in LPT and in full N-body fields, respectively. We denote by $\mathcal{P}_\delta$ the corresponding pdfs for the Eulerian density contrast.

In figure 2.11, we show the pdfs of ψ for the ZA, 2LPT and full N-body gravity. The most important feature of ψ is that, whatever the model for structure formation, the pdf exhibits reduced non-Gaussianity compared to the pdf for the density contrast δ (see the upper panel of figure 2.1 for comparison). The main reason is that $\mathcal{P}_\delta$, unlike $\mathcal{P}_\psi$, is tied down to zero at $\delta = -1$. It is highly non-Gaussian in the final conditions, both in N-body simulations and in approximations to the true dynamics. For a quantitative analysis, we looked at the first and second-order non-Gaussianity statistics: the skewness γ_1 and the excess kurtosis γ_2,

$$\gamma_1 \equiv \frac{\mu_3}{\sigma^3} \quad \text{and} \quad \gamma_2 \equiv \frac{\mu_4}{\sigma^4} - 3, \tag{2.5}$$

where μ_n is the n-th moment about the mean and σ is the standard deviation. We estimated γ_1 and γ_2 at redshift zero in our simulations, in the one-point statistics of the density contrast δ and of the divergence of the displacement field ψ. The results are shown in table 2.1. In all cases, we found that both γ_1 and γ_2 are much smaller when measured from $\mathcal{P}_\psi$ instead of $\mathcal{P}_\delta$.

At linear order in Lagrangian perturbation theory (the Zel'dovich approximation), the divergence of the displacement field is proportional to the density contrast in the initial conditions, $\delta(\mathbf{q})$, scaling with the negative growth factor, $-D_1(\tau)$:

$$\psi^{(1)}(\mathbf{q}, \tau) = \nabla_{\mathbf{q}} \cdot \mathbf{\Psi}^{(1)}(\mathbf{q}, \tau) = -D_1(\tau)\, \delta(\mathbf{q}). \tag{2.6}$$

Since we take Gaussian initial conditions, the pdf for ψ is Gaussian at any time with the ZA. In full gravity, non-linear evolution slightly breaks Gaussianity. $\mathcal{P}_{\psi,\mathrm{Nbody}}$ is slightly skewed towards negative values while its mode gets shifted around $\psi \approx 1$. Taking into account non-local effects, 2LPT tries to get closer to the shape observed in N-body simulations, but the correct skewness is overshot and the pdf is exceedingly peaked.

Figure 2.12 shows a slice of the divergence of the displacement field, measured at redshift zero for particles occupying a flat 512^2-pixel Lagrangian sheet from one of our simulations. For comparison, see also the figures in Mohayaee *et al.* (2006); Pueblas & Scoccimarro (2009) and Neyrinck (2013). We used the color scheme of the latter paper, suggesting a topographical analogy when working in Lagrangian coordinates. As structures take shape, ψ departs from its initial value; it takes positive values in underdensities and negative values in overdensities. The shape of voids (the "mountains") is found to be reasonably similar in LPT and in the N-body simulation. For this reason, the influence of late-time non-linear effects in voids is milder as compared to overdense structures, which makes them easier to relate to the initial conditions. However, in overdense regions where ψ decreases, it is not allowed to take arbitrary values: where gravitational collapse occurs, "lakes" form and ψ gets stuck around a collapse barrier, $\psi \approx -3$. As expected, these "lakes", corresponding to virialized clusters, can only be found in N-body simulations, since LPT fails to accurately describe the highly non-linear physics involved. A small bump at $\psi = -3$ is visible in $\mathcal{P}_{\psi,\mathrm{Nbody}}$ (see figure 2.11). We checked that this bump gets more visible in higher mass-resolution simulations (200 Mpc/h box for 256^3 particles), where matter is more clustered. This means that part of the information about gravitational clustering can be found in the one-point statistics of ψ. Of course, the complete description of halos requires to precisely account for the shape of the "lakes", which can only be done via higher-order correlation functions. More generally, it is possible to use Lagrangian information in order to classify structures of the cosmic web. In particular, DIVA (Lavaux & Wandelt, 2010) uses the shear of the displacement field and ORIGAMI (Falck, Neyrinck & Szalay, 2012) the number of phase-space folds. While these techniques cannot be straightforwardly used for the analysis of galaxy surveys, where we lack Lagrangian information, recently proposed techniques for physical inference of the initial conditions (chapters 4 and 5 Jasche & Wandelt, 2013a; Jasche, Leclercq & Wandelt, 2015) should allow their use with observational data.

Figure 2.13 shows two-dimensional histograms comparing N-body simulations to the LPT realizations for the density contrast δ and the divergence of the displacement field ψ. At this point, it is useful to note that a good mapping exists in the case where the relation shown is monotonic and the scatter is narrow. As pointed out by Sahni & Shandarin (1996) and Neyrinck (2013), matter in the substructure of 2LPT-voids has incorrect statistical properties: there are overdense particles in the low density region of the 2LPT δ-scatter plot. This degeneracy is also visible in the $\psi > 0$ region of the 2LPT ψ-scatter plot. On average, the scatter is bigger with ψ than with δ, in particular in overdensities ($\psi < 0$), since with LPT, particles do not cluster: ψ takes any value between 2 and -3 where it should remain around -3.

Summing up our discussions in this paragraph, we analyzed the relative merits of the Lagrangian divergence of the displacement field ψ, and the Eulerian density contrast δ at the level of one-point statistics. The important differences are the following:

1. $\boldsymbol{\Psi}$ being irrotational up to order two, its divergence ψ contains nearly all information on the displacement field in one dimension, instead of three. The collapse barrier at $\psi = -3$ is visible in $\mathcal{P}_\psi$ for N-body simulations but not for LPT. A part of the information about non-linear gravitational clustering is therefore encoded in the one-point statistics of ψ.

2. ψ exhibits much fewer gravitationally-induced non-Gaussian features than δ in the final conditions (figure 2.11 and table 2.1).

3. However, the values of ψ are more scattered than the values of δ with respect to the true dynamics (figure 2.13), meaning that an unambiguous mapping is more difficult.

2.2.2 Perturbative and non-perturbative prescriptions for ψ

Even if ψ does not contain all the information about the vector displacement field $\boldsymbol{\Psi}$, knowledge of its evolution allows for methods to produce approximate particle realizations at the desired redshift, for the variety of cosmological applications described in the introduction of this thesis. These methods include, but are not limited to, the ZA and 2LPT. On the contrary, 3LPT involves a non-zero rotational component and comes at the expense of significantly greater complexity, for an agreement with full gravity that does not improve substantially (Buchert, Melott & Weiß, 1994; Bouchet *et al.*, 1995; Sahni & Shandarin, 1996). Since we have adopted the approximation that the displacement field is potential, we stop our analysis of LPT at second order. However, we will describe various non-perturbative schemes.

Importantly, ψ-based methods are essentially as fast as producing initial conditions for N-body simulations. Their implementation can be decomposed in several steps:

1. Generation of a voxel-wise initial-density field δ. It is typically a grf, given a prescription for the linear power spectrum (see section B.6), but it can also include primordial non-Gaussianities.

2. Estimation of ψ from δ at the desired redshift.

3. Generation of the final vector displacement field $\boldsymbol{\Psi}$ from ψ with an inverse-divergence operator.

4. Application of $\boldsymbol{\Psi}$ to the particles of a regular Lagrangian lattice to get their final positions.

In practice, steps 1 and 3 are performed in Fourier space, using fast Fourier transforms to translate between configuration space and Fourier space when necessary. In the remainder of this paragraph, we review various prescriptions that have been proposed in the literature to estimate $\psi(\mathbf{q},\tau)$ from $\delta(\mathbf{q})$ (step 2).

The Zel'dovich approximation. The first scheme, already studied in section 1.5.2, is the ZA (equation (1.128)),

$$\psi_{\mathrm{ZA}}(\mathbf{q},\tau) = -D_1(\tau)\,\delta(\mathbf{q}) \equiv -\delta_{\mathrm{L}}(\mathbf{q},\tau). \tag{2.7}$$

The ZA allows to separate prescriptions for ψ into two classes: *local* Lagrangian approximations, where ψ depends only on its linear value, $\psi_{\mathrm{L}}(\mathbf{q},\tau) \equiv -\delta_{\mathrm{L}}(\mathbf{q},\tau)$ and *non-local* ones (e.g. higher-order LPT) where ψ depends on derivatives of ψ_{L} as well (which means that the behavior of a Lagrangian particle depends on its neighbours).

Second-order Lagrangian perturbation theory. In 2LPT, the non-local prescription for ψ is (see equation (1.133))

$$\psi_{\mathrm{2LPT}}(\mathbf{q},\tau) = -D_1(\tau)\Delta_{\mathbf{q}}\phi^{(1)}(\mathbf{q}) + D_2(\tau)\Delta_{\mathbf{q}}\phi^{(2)}(\mathbf{q}), \tag{2.8}$$

where the Lagrangian potentials follow the Poisson-like equations (1.134) and (1.135). As pointed out by Neyrinck (2013), since 2LPT is a second-order scheme, ψ_{2LPT} is roughly parabolic in the local δ_{L}, which yields, using $D_2(\tau) \approx -\frac{3}{7}D_1^2(\tau)$ (Bouchet *et al.*, 1995),

$$\psi_{\mathrm{2LPT}}(\mathbf{q},\tau) \approx \psi_{\mathrm{2LPT,parab}}(\mathbf{q},\tau) \equiv -\delta_{\mathrm{L}}(\mathbf{q},\tau) + \frac{1}{7}\left(\delta_{\mathrm{L}}(\mathbf{q},\tau)\right)^2 . \tag{2.9}$$

The spherical collapse approximation. Bernardeau (1994) provides a simple formula for the time-evolution (collapse or expansion) of a spherical Lagrangian volume element, independent of cosmological parameters:

$$V(\mathbf{q},\tau) = V(\mathbf{q})\left(1 - \frac{2}{3}\delta_{\mathrm{L}}(\mathbf{q},\tau)\right)^{3/2} . \tag{2.10}$$

Building upon this result, Mohayaee *et al.* (2006); Lavaux (2008) and Neyrinck (2013) derived a prescription for the divergence of the displacement field. Considering the isotropic stretch of a Lagrangian mass element that occupies a cube of side length $1 + \psi/3$ (giving $\nabla_{\mathbf{q}} \cdot \mathbf{\Psi} = \psi$), mass conservation imposes

$$\frac{V(\mathbf{q},\tau)}{V(\mathbf{q})} = \frac{1}{1+\delta} = \left(1 + \frac{\psi}{3}\right)^3 . \tag{2.11}$$

Equations (2.10) and (2.11) yield

$$\psi = 3\left(\sqrt{1 - \frac{2}{3}\delta_{\mathrm{L}}} - 1\right) . \tag{2.12}$$

However, there exists no solution for $\delta_{\mathrm{L}} > 3/2$. Neyrinck (2013) proposes to fix $\psi = -3$ in such volume elements. This corresponds to the ideal case of a Lagrangian patch contracting to a single point ($\nabla_{\mathbf{q}} \cdot \mathbf{x} = 0$). The final prescription for the spherical collapse (SC) approximation is then

$$\psi_{\mathrm{SC}}(\mathbf{q},\tau) = \begin{cases} 3\left(\sqrt{1 - \frac{2}{3}\delta_{\mathrm{L}}(\mathbf{q},\tau)} - 1\right) & \text{if } \delta_{\mathrm{L}} < 3/2, \\ -3 & \text{if } \delta_{\mathrm{L}} \geq 3/2. \end{cases} \tag{2.13}$$

One possible concern with this formula is that, in full gravity, there are roughly as many particles with $\psi > -3$ as with $\psi < -3$ (see e.g. trajectories in ψ as a function of the scale factor a, figure 7 in Neyrinck, 2013). Yet, this remains more correct than what happens with LPT, where ψ can take any negative value, indicating severe unphysical over-crossing of particles in collapsed structures.

Compared to LPT, the SC approximation gives reduced stream-crossing, better small-scale flows and one-point pdf correspondence to the results of full gravity. However, a significant drawback is its incorrect treatment of large-scale flows, leading to a negative offset in the large-scale power spectrum (figure 14 in Neyrinck, 2013).[2] LPT realizations, on the other hand, give more accurate large-scale power spectra, as well as improved cross-correlation to the density field evolved with full gravity.

Local Lagrangian approximations. The SC approximation belongs to a more general family of "local Lagrangian" approximations investigated by Protogeros & Scherrer (1997), parameterized by $1 \leq \alpha \leq 3$, the effective number of axes along which the considered volume element undergoes gravitational collapse. The corresponding density is given by

$$\delta_\alpha(\psi) = \left(1 + \frac{\psi}{\alpha}\right)^{-\alpha} - 1. \tag{2.14}$$

[2] An empirical correction may be added to the SC formula to fix this issue: multiplying δ_{L} in equation (2.13) by a factor such that the large-scale power spectrum of SC realizations agrees with that of LPT realizations (Neyrinck, 2013). See also the paragraph on MUSCLE.

Here, ψ is the actual non-linear displacement-divergence of a volume element, not necessarily related to the linearly evolved ψ_L. From equations (2.10) and (2.11), we get

$$\delta = \left(1 - \frac{2}{3}\delta_\mathrm{L}\right)^{-3/2} - 1 = \left(1 + \frac{2}{3}\psi_\mathrm{L}\right)^{-3/2} - 1, \tag{2.15}$$

therefore the spherical collapse approximation corresponds to the case $\alpha = 3/2$ for $\psi = \psi_\mathrm{L}$. The cubic mass-element approximation that would follow directly from using equation (2.11) without equation (2.10) corresponds to the case $\alpha = 3$ for the full ψ. Neyrinck (2013) shows that the δ–ψ relation closely follows $\delta_3(\psi)$ for $\psi < 0$, whereas for $\psi > 0$ the result is between $\delta_3(\psi)$ and $\delta_{3/2}(\psi)$, when accounting for the anisotropy of gravitational expansion.

Augmented Lagrangian Perturbation Theory. As discussed before, LPT correctly describes large scales and SC more accurately captures small, collapsed structures. Kitaura & Heß (2013) proposed a recipe to interpolate between the LPT displacement on large scales and the SC displacement on small scales, calling it Augmented Lagrangian Perturbation Theory (ALPT). It reads

$$\psi_\mathrm{ALPT}(\mathbf{q},\tau) = (K_{R_\mathrm{s}} * \psi_\mathrm{2LPT})(\mathbf{q},\tau) + [(1 - K_{R_\mathrm{s}}) * \psi_\mathrm{SC}](\mathbf{q},\tau), \tag{2.16}$$

or, in Lagrangian Fourier space,[3]

$$\psi_\mathrm{ALPT}(\boldsymbol{\kappa},\tau) = K_{R_\mathrm{s}}(\kappa)\, \psi_\mathrm{2LPT}(\boldsymbol{\kappa},\tau) + [1 - K_{R_\mathrm{s}}(\kappa)]\, \psi_\mathrm{SC}(\boldsymbol{\kappa},\tau). \tag{2.17}$$

This method introduces a free parameter, R_s, the width of the Gaussian kernel used in the above equations to filter between large and small displacements, $K_{R_\mathrm{s}}(k) \propto \exp(-k^2/2 \times (R_\mathrm{s}/2\pi)^2)$. In numerical experiments, Kitaura & Heß (2013) empirically found that the range $R_\mathrm{s} = 4-5$ Mpc/h yields the best density cross-correlation to full gravity.

Multi-scale spherical collapse evolution. Neyrinck (2016) argued that the major deficiency in the SC approximation is its treatment of the void-in-cloud process (in the terminology originally introduced by Sheth & van de Weygaert, 2004), i.e. of small underdensities in larger-scale overdensities. Such regions should eventually collapse, which is not accounted for in SC. To overcome this problem, he proposes to use the SC prescription as a function of the initial density contrast on multiple Gaussian-smoothed scales, thus including the void-in-cloud process. The resulting parameter-free scheme, MUSCLE (MUltiscale Spherical-CoLlapse Evolution), mathematically reads

$$\psi_\mathrm{MUSCLE}(\mathbf{q},\tau) = \begin{cases} 3\left(\sqrt{1 - \frac{2}{3}\delta_\mathrm{L}(\mathbf{q},\tau)} - 1\right) & \text{if } \delta_\mathrm{L} < 3/2 \text{ and } \forall R_\mathrm{s} \geq R_\mathrm{i}, K_{R_\mathrm{s}} * \delta_\mathrm{L} < 3/2, \\ -3 & \text{otherwise,} \end{cases} \tag{2.18}$$

where R_i is the resolution of the initial density field $\delta(\mathbf{q})$, and $K_{R_\mathrm{s}} * \delta_\mathrm{L}$ is the linearly extrapolated initial density field, smoothed using a Gaussian kernel of width R_s. In practice, a finite number of scales $r > R_\mathrm{i}$ have to be tried (for example $r = 2^n R_\mathrm{i}$ for integers $0 \leq n \leq n_\mathrm{max}$ such that $2^{n_\mathrm{max}} R_\mathrm{i} \leq L$ and $2^{n_\mathrm{max}+1} R_\mathrm{i} > L$).

Neyrinck (2016) checked that MUSCLE corrects the problems of SC at large scales and outperforms the ZA and 2LPT in terms of the density cross-correlation to full gravity.

2.2.3 Non-linear evolution of ψ and generation of a vector part

Beyond the approximations presented in the previous section, Chan (2014) analyzed the non-linear evolution of $\boldsymbol{\Psi}$ in full gravity, splitting it into its scalar and vector parts (the so-called "Helmholtz decomposition"):

$$\boldsymbol{\Psi}(\mathbf{q}) = \nabla_\mathbf{q}\phi(\mathbf{q}) + \nabla_\mathbf{q} \times \mathbf{A}(\mathbf{q}), \tag{2.19}$$

with

$$\Delta_\mathbf{q}\phi = \nabla_\mathbf{q} \cdot \boldsymbol{\Psi}(\mathbf{q}), \tag{2.20}$$
$$\Delta_\mathbf{q}\mathbf{A}(\mathbf{q}) = -\nabla_\mathbf{q} \times \boldsymbol{\Psi}(\mathbf{q}). \tag{2.21}$$

[3] We denote by $\boldsymbol{\kappa}$ a Fourier mode on the Lagrangian grid, κ its norm.

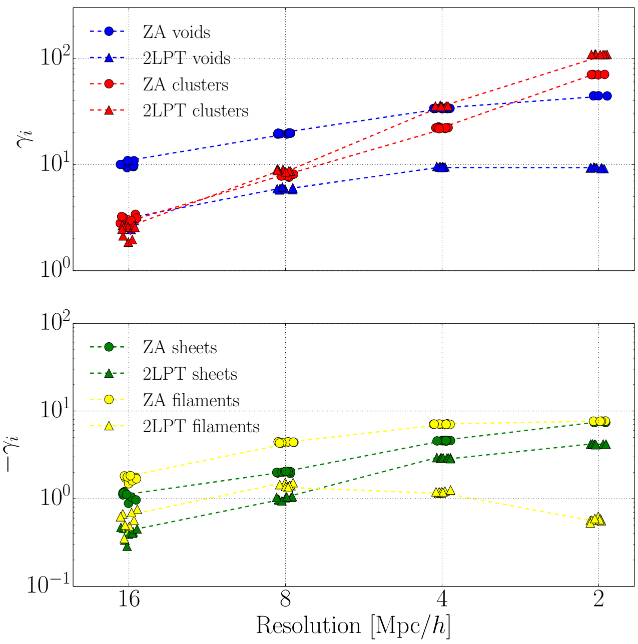

Figure 2.14: Relative volume fraction of voids, sheets, filaments and clusters predicted by LPT, compared to N-body simulations, as a function of the resolution used for the definition of the density fields. The points are sightly randomized on the x-axis for clarity. The estimators γ_i are defined by eq (2.22). Eight realizations of the ZA (circles) and 2LPT (triangles) are compared to the corresponding N-body realization, for various resolutions. The volume fraction of incorrectly predicted structures in LPT generally increases with increasing resolution.

Looking at two-point statistics of $\mathbf{\Psi}$, he found that shell-crossing leads to a suppression of small-scale power in the scalar part, and, subdominantly, to the generation of a vector contribution. Even at late-time and non-linear scales, the scalar part of the displacement field remains the dominant contribution. The rotational component is much smaller and does not have a coherent large-scale component. Therefore, the potential approximation is still good even when shell-crossing is non-negligible.

However, as pointed out by Neyrinck (2016), even if we neglect the rotational component, there is still a long way to go before we can perfectly predict ψ. Variants of LPT, such as ALPT (primarily motivated by the agreement in the scatter plot of final versus initial ψ – see figure 6 in Neyrinck, 2013 and figure 10 in Chan, 2014) or the inclusion of a suppression factor in the LPT displacement potential (Chan, 2014 – designed for fitting the non-linear power spectrum of $\mathbf{\Psi}$) extract information from simulations by taking the average of some statistics. Since shell-crossing is a highly non-linear process, it may not be surprising that such approaches yield limited success compared to standard LPT for some other statistics (such as the density power spectrum or phase accuracy). This suggests that a more detailed understanding and modeling of the small-scale physics beyond the simple phenomenological approach is required for improvement in ψ-based schemes, which would substantially increase the accuracy of particle realizations.

2.3 Comparison of structure types in LPT and N-body dynamics

This section draws from section II.B. in Leclercq *et al.* (2013).

In this section, we perform a study of differences in structure types in density fields predicted by LPT and N-body simulations. We employ the web-type classification algorithm proposed by Hahn *et al.* (2007a), which relies on estimating the eigenvalues of the Hessian of the gravitational potential (see section C.2). This algorithm dissects the voxels into four different web types (voids, sheets, filaments and clusters). Due to the different representations of the non-linear regime of structure formation, we expect differences in structure types in LPT and N-body simulations. In particular, overdense clusters are objects in the strongly non-linear regime, far beyond shell-crossing, where predictions of LPT fail, while underdense voids are believed to be better apprehended (e.g. Bernardeau *et al.*, 2002).

As an indicator of the mismatch between the volume occupied by different structure types in LPT and N-body dynamics, we use the quantities γ_i defined by

$$\gamma_i \equiv \frac{N_i^{\mathrm{LPT}} - N_i^{\mathrm{Nbody}}}{N_i^{\mathrm{Nbody}}}, \tag{2.22}$$

where i indexes one of the four structure types (T_0 = void, T_1 = sheet, T_2 = filament, T_3 = cluster), and N_i^{LPT} and N_i^{Nbody} are the numbers of voxels flagged as belonging to a structure of type T_i, in corresponding LPT and in N-body realizations, respectively. At fixed resolution, corresponding realizations have the same total number of voxels N_{tot}, so we also have

$$\gamma_i = \frac{\mathrm{VFF}_i^{\mathrm{LPT}}}{\mathrm{VFF}_i^{\mathrm{Nbody}}} - 1, \tag{2.23}$$

where the volume filling fraction of structure type T_i is defined by $\mathrm{VFF}_i \equiv N_i/N_{\mathrm{tot}}$.

In figure 2.14, we plot γ_i as a function of the voxel size used to define the density fields. γ_i is positive for clusters and voids, and negative for sheets and filaments, meaning that too large cluster and void regions are predicted in LPT, at the detriment of sheets and filaments. More specifically, LPT predicts fuzzier halos than N-body dynamics, and incorrectly predicts the surroundings of voids as part of them. This result indicates that even though LPT and N-body fields look visually similar, there are crucial differences in the representation of structure types. As demonstrated by figure 2.14, this mismatch increases with increasing resolution. This effect is of general interest when employing LPT in LSS data analysis.